

Representations and Strategies for Transferable Machine Learning Models in Chemical Discovery

Daniel R. Harper^{1,2,#}, Aditya Nandy^{1,2,#}, Naveen Arunachalam¹, Chenru Duan^{1,2}, Jon Paul Janet¹,
and Heather J. Kulik^{1,*}

¹*Department of Chemical Engineering, Massachusetts Institute of Technology, Cambridge, MA
02139*

²*Department of Chemistry, Massachusetts Institute of Technology, Cambridge, MA 02139*

[#]These authors contributed equally.

ABSTRACT: Strategies for machine-learning(ML)-accelerated discovery that are general across materials composition spaces are essential, but demonstrations of ML have been primarily limited to narrow composition variations. By addressing the scarcity of data in promising regions of chemical space for challenging targets like open-shell transition-metal complexes, general representations and transferable ML models that leverage known relationships in existing data will accelerate discovery. Over a large set (ca. 1000) of isovalent transition-metal complexes, we quantify evident relationships for different properties (i.e., spin-splitting and ligand dissociation) between rows of the periodic table (i.e., $3d/4d$ metals and $2p/3p$ ligands). We demonstrate an extension to graph-based revised autocorrelation (RAC) representation (i.e., eRAC) that incorporates the effective nuclear charge alongside the nuclear charge heuristic that otherwise overestimates dissimilarity of isovalent complexes. To address the common challenge of discovery in a new space where data is limited, we introduce a transfer learning approach in which we seed models trained on a large amount of data from one row of the periodic table with a small number of data points from the additional row. We demonstrate the synergistic value of the eRACs alongside this transfer learning strategy to consistently improve model performance. Analysis of these models highlights how the approach succeeds by reordering the distances between complexes to be more consistent with the periodic table, a property we expect to be broadly useful for other materials domains.

1. Introduction.

Machine learning (ML) models have been demonstrated as a powerful alternative to conventional computational high-throughput screening¹⁻² by greatly accelerating chemical discovery³⁻⁸, e.g., with active learning.⁹⁻¹² It is typically the case at the outset of a discovery campaign that a great deal is known from experiments, computation, and associated ML models about a highly localized region of chemical space, but the most promising directions for improvement lie outside this region. For example, many of the most active catalysts¹³⁻¹⁴ or single molecule magnets¹⁵⁻¹⁶ require the use of rare and toxic *4d* or *5d* metals, and identification of principles¹⁷ for their replacement with *3d* metals would be advantageous¹⁸⁻¹⁹ in a number of difficult small molecule catalytic conversions (e.g., H₂²⁰⁻²⁵, CO₂²⁶, and O₂²⁷). Thus, ML-accelerated discovery requires models and representations that generalize well and strategies to exploit existing knowledge while data in new regions is scarce.

Despite the need for ML models that generalize across the periodic table^{3, 28-31}, ML models have much more commonly been applied in narrow regions of chemical space, such as closed-shell organic (i.e., CHNOF-containing) molecules in the QM9 dataset³², with few exceptions³³. For open-shell transition-metal chemistry in particular, unique challenges are present in the generation of sufficiently large data sets for ML model training while spanning a large range of metal centers, ligand chemistry, and the cooperative effect the metal/ligand identity play in the resulting spin or oxidation state of the complex.³⁴ While ML-model-accelerated computational discovery has targeted numerous transition-metal catalysts³⁵⁻³⁹ or functional complexes^{9, 40} and related metal-organic materials (e.g., metal-organic frameworks⁴¹⁻⁴³ and transition metal oxides⁴⁴), these models have also generally been restricted to a small number of transition metals or modest modifications of the ligands. While only preliminarily

demonstrated on open-shell transition-metal complexes⁴⁵⁻⁴⁷, there is evidence that electronic descriptors such as partial charges or bond valence⁴⁵ and molecular orbitals^{46, 48-49} or other computed electronic properties⁵⁰⁻⁵¹ are one path to training transferable ML models on small data sets. Sidestepping ML with direct, computationally demanding simulation (e.g., with density functional theory or DFT) in large spaces of functional materials and catalysts^{34, 52} is plagued by combinatorial challenges^{34, 52-54} that can only be partly reduced through inverse design strategies (e.g., with alchemical derivatives⁵⁴⁻⁵⁷ or heuristics⁵⁸). Nevertheless, all such approaches that require an electronic structure calculation to be completed for property prediction or optimization hamper the large-scale exploration that is required for large-scale materials discovery.

For transferable ML models, opportunities and challenges for either conventional 3D-structure-based⁵⁹⁻⁶³ or graph-based⁶⁴⁻⁶⁶ representations remain. Here, we focus on graph-based revised autocorrelations^{65, 67-68} (RACs⁶⁵) that are no-cost products and differences of heuristic atomic properties (e.g., nuclear charge or Pauling electronegativity) on the molecular graph. The 155-feature form of RACs (i.e., RAC-155⁶⁵) was used⁹ to train a multi-task artificial neural network (ANN) that accelerated identification of soluble and high redox potential TMCs for redox flow batteries from nearly 3M candidates in weeks instead of decades.⁹ In this or other discovery campaigns for which there is a reasonable degree of similarity between training and test data, RAC-155 and its feature-selected subsets have been used^{9, 35, 38, 65, 69-72} to train ML (e.g., kernel ridge regression, KRR, and ANN) models that exhibit good performance on modestly sized (ca. 200–1000 data points) data sets of DFT properties for TMCs, including around 1–4 kcal/mol accuracy for adiabatic spin-splitting energies^{65, 71}, bond lengths^{65, 69, 73}, ionization/redox potentials⁶⁵, HOMO energies,⁷⁰ and catalytic properties.³⁸

Exemplary of how RAC-trained models have limited domains of applicability, Janet et al.

observed⁷¹ that introducing new elements (e.g., P or As) into an out-of-distribution test molecule uniquely challenged ANN models trained only on first-row, *3d* open-shell transition-metal complexes with primarily *2p* ligand chemistry. Conversely, introducing diverse metal coordination environments with a wider range of sampled elements into model training greatly improved ANN model generalization⁷⁴, reducing mean absolute errors by around 25–30%. Because distance in feature space (e.g., in KRR) or latent space (i.e., in the ANN) is a critical component, prediction by ML models of new materials with compositions not well supported by training data is universally challenging. Nevertheless, RACs and other widely used representations⁶⁰ employ the nuclear charge in the representation, exaggerating differences between rows of the periodic table with respect to differences in group number⁷⁵. While some heuristic properties in RACs (e.g., the Pauling electronegativity) more faithfully encode chemical similarity⁶⁴, the nuclear-charge-based features are often emphasized in feature-selected subsets, highlighting their importance in model prediction.⁶⁹

Limitations in the representation will make it challenging for an ML model to learn relationships between isovalent materials with elements from different rows of the periodic table, despite clear relationships⁷⁶⁻⁷⁸ in both ligand field strength (e.g., *3p* P > S and *2p* N > O) and *d*-filling trends of spin-splitting energies⁷⁹ between *3d* and *4d* TMCs. One may anticipate that changing the row of the metal requires a change in the ligand chemical composition (e.g., for nitrogen-coordinating ligands vs phosphorus-coordinating ligands) as well. The existence of these structure-property relationships presents an opportunity for representation improvement. In this work, we tackle the challenge of improving the transferability of no-cost representations by introducing effective nuclear charge as a heuristic into RACs, an approach previously demonstrated only in closed-shell organic molecules⁸⁰⁻⁸¹ or in metallic alloys^{33, 82}. We show how

this always improves model performance and devise a synergistic strategy for leveraging large amounts of data containing elements from one row of the periodic table to improve the learning curves on materials belonging to a new target row. While demonstrated here on $3d/4d$ and $2p/3p$ learning tasks, we expect this approach to be broadly useful for other materials.

2. Approach.

2a. Dataset Construction.

Mononuclear, octahedral TMCs were assembled from combinations of eight transition metals with ten small, common ligands to explore relationships among isovalent metal centers and metal-coordinating ligand atoms. While the electronic structure of some of these TMCs were discussed in Ref. ⁷⁹, we reiterate the rationale for their curation in paired datasets for ML on isovalent properties here. The TMCs contain $3d$ or $4d$ mid-row transition metals (Cr/Mo, Mn/Tc, Fe/Ru, and Co/Rh) in +2 and +3 oxidation states (Figure 1). We study the energetically accessible spin states for these metals, which correspond to low-spin (LS), intermediate-spin (IS), and high-spin (HS) states, where the IS and HS states differ by having two more or four more unpaired electrons, respectively, with respect to the singlet or doublet LS state. The earliest Cr(III)/Mo(III) or latest Co(II)/Rh(II) are studied in only two states, a LS doublet and an IS quartet (Supporting Information Table S1).

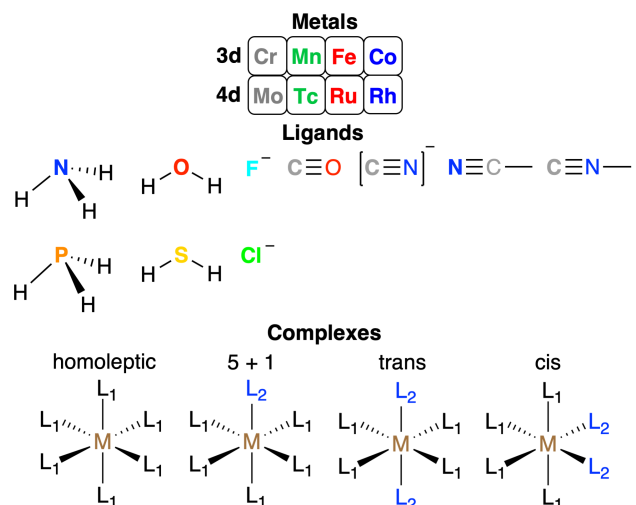


Figure 1. Overview of eight metals and ten ligands used to form mononuclear, octahedral transition-metal complexes in the data sets in this work. (top) 3d and 4d metals grouped by row and column order in the periodic table. (middle) Skeletal structures of the ten ligands with the metal-coordinating atom shown in bold. The six left-most ligands are grouped by isovalent 2*p* metal-coordinating atoms in the first row (i.e., N, O, and F) with 3*p* metal-coordinating atoms in the second row (P, S, and Cl). Four additional ligands that have carbon or nitrogen coordinating atoms are depicted at right. (bottom) Symmetries of transition-metal complexes studied by assembling up to two ligand types (*L*₁ in black and *L*₂ in blue) in octahedral complexes: homoleptic (*L*₁ = *L*₂), 5+1 (a single axial *L*₂), and trans or cis placement of two *L*₂ ligands.

The ten common ligands were selected for their varying field strengths (i.e., from weak field halides to strong field carbonyl). Six (i.e., three pairs) of these ligands contain isovalent coordinating atoms that differ in principal quantum number, e.g., 2*p* vs. 3*p* NH₃ and PH₃ (Figure 1). A large set of possible TMC isomers were assembled from up to two of these ligands (i.e., *L*₁ and *L*₂) in four arrangements: i) homoleptic M(*L*₁)₆; ii) trans M(*L*₁)₄(*L*₂)₂; iii) cis M(*L*₁)₄(*L*₂)₂; and iv) 5+1 M(*L*₁)₅(*L*₂) (Figure 1). All homoleptic (i.e., 440) TMCs and trans or 5+1 (i.e., 3,960 each) structures were set up for calculation with DFT, whereas only a subset (1,080) of the cis structures were set up (see Sec. 3a and Supporting Information Table S2). For the TMCs in this set, we compute (see Sec. 3a) up to three gas-phase, adiabatic spin-splitting energies, i.e., between the LS and HS states, $\Delta E_{\text{H-L}}$, as well as between the IS state and either the LS or the HS state (i.e., $\Delta E_{\text{H-I}}$ and $\Delta E_{\text{I-L}}$), which were discussed in part in Ref. ⁷⁹. In this work, for a subset of

the TMCs, we now also compute a vertical ligand dissociation (LD) energy, ΔE_{LD} , the energy required to rigidly remove a single axial ligand (see Sec. 3a).

From nearly ten thousand hypothetical TMCs, we obtain a smaller subset for testing the transferability of ML models by pairing isovalent species with differing principal quantum numbers via a filtering procedure that is more restrictive than that used in Ref. ⁷⁹. For the isovalent metal pairing (IMP) set, we compare computed properties of pairs of complexes that have metal centers in the same group of the periodic table but differ in their principal quantum number (e.g., $3d$ Fe(II) and $4d$ Ru(II)) with identical characteristics for all other TMC properties (e.g., spin multiplicity, L_1/L_2 ligands, and symmetry class). After accounting for data fidelity and convergence rates, we obtain over 1200 pairs of spin-splitting ΔE values depending on the spin states compared, with the I-L set roughly twice as large as the H-L or H-I sets. The IMP set of ΔE_{LD} values across spin states contains over 1000 pairs (Supporting Information Table S3).

We also construct an isovalent ligand pairing (ILP) set, which compares properties of pairs of TMCs that have ligands with metal-coordinating atoms that belong to the same group of the periodic table but differ in principal quantum number (e.g., $2p$ N and $3p$ P). Because only six of the ten ligands belong to one of these $2p/3p$ pairs, heteroleptic TMCs could include between zero and two unique ligands from this subset. For the pairs in the ILP set, we change all relevant ligands simultaneously while holding any incompatible ligands and all other TMC properties (e.g. metal, oxidation and spin state) fixed. Because we start from a smaller subset of TMCs that have the relevant ligands, ILP subsets of spin-splitting and ligand dissociation energies are about half of the size of the IMP sets (Supporting Information Table S4).

2b. Representations.

We employ Moreau-Broto autocorrelations (ACs)^{67, 83} and revised AC variants (i.e.,

RACs)⁶⁵, which are representations formed by discrete operations on the heuristic properties of atoms in the molecular graph in analogy to continuous autocorrelations. A standard AC is evaluated over all of the n atoms in a molecule that are d bonds apart:

$$P_d = \sum_i \sum_j^{start\ scope} P_i P_j \delta(d_{ij}, d) \quad (1)$$

where P is the chosen property, P_i and P_j are the specific values of the i th and j th atoms that are d_{ij} bonds apart. The five heuristic properties^{65, 67-68, 83-84} we have employed for transition-metal chemistry^{65, 84} include: the Pauling electronegativity, nuclear charge, covalent radius, topology, and the identity (i.e., 1) and produce a $5d+5$ dimensional vector. ACs have achieved best-in-class performance for geometry-free descriptor predictions of atomization energies on subsets of QM9³² using KRR⁶⁵ or ANN models⁷¹ with diminishing returns observed for depth cutoffs above three⁶⁵, although higher depth cutoffs are sometimes used^{68, 84}.

Extensions of ACs to enrich metal-local descriptors⁸⁵ in the feature vector led to the development of RACs, as first introduced in Ref. ⁶⁵. RACs include centering (i.e., always including in the sum) the property evaluation on the metal (i.e., mc-RACs) or the ligand atom that coordinates the metal (i.e., lc-RACs). The lc-RACs are averaged separately over ligands of specific types, which were referred to as the scope in Ref. ⁶⁵. In the octahedral complexes studied here, lc-RACs are averaged separately over the equatorial or axial ligands. RACs also introduced the difference of two atomic properties:

$$P'_d = \sum_i \sum_j^{start\ scope} (P_i - P_j) \delta(d_{ij}, d) \quad (2)$$

which can be non-trivially computed for metal-centered or ligand-centered RACs excluding the identity property for any $d > 0$ bond paths. In total, the complete RAC set evaluated on the five

original heuristic properties consists of $30d+30$ product-based and $12d$ difference-based RACs for a total feature vector size of $42d+30$. For a typical⁶⁵ cutoff of $d = 3$, this yields 156 possible features. For the mononuclear octahedral TMCs that are the focus of this work, excluding five constant features (i.e., corresponding to connectivity around the metal center) produces 151 features. In the original work, four additional descriptors of ligand denticity, oxidation state, spin state, and Hartree–Fock exchange fraction in the DFT functional were added, leading to the name RAC-155⁶⁵. In this work, we always include the oxidation state (i.e., for 152 total features) and the spin state is included only for ΔE_{LD} (i.e., for 153 total features) but still refer to the set as RAC-155.

Because RAC heuristic properties depend on the properties of individual atoms, we revisit the extent to which such properties encode useful information about chemical similarity of distinct elements. Some, such as the Pauling electronegativity, encode close chemical similarity of distinct elements (e.g., χ : 1.88 for Co vs 1.90 for Tc). Still, the nuclear charge, Z , exaggerates the dissimilarity of elements with differing principal quantum number belonging to the same group (e.g., Z : 27 for Co vs 45 for Rh or 7 for N vs 15 for P). Thus, we expect low-complexity kernel models trained on RAC-155 to exaggerate differences in TMCs with metals or ligands from differing rows of the periodic table in comparison to those from the same row. To illustrate this, we carried out principal component analysis (PCA) on a subset (i.e., $d = 0$ or 1) of mc-RACs in RAC-155 applied to all IMP (i.e., with both $3d$ and $4d$ metals) complexes for which we have computed the ΔE_{I-L} property. For these TMCs, the first PC in this subset of RAC-155 primarily distinguishes the metal centers (Figure 2). Not only are $3d$ and $4d$ metals very distant from each other, but the strong variation of the metal Z over the set in comparison to the other heuristics leads to the later $3d$ Co being the most proximal metal to the early $4d$ Mo.

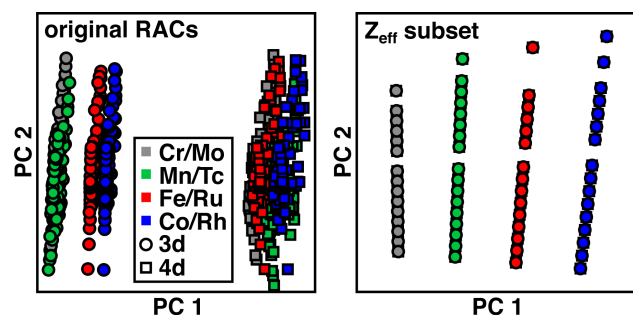


Figure 2. PCA obtained using the subset of features in RAC-155 that are metal-centered and $d = 0$ or 1 (left) and using only the metal-centered RACs of the Z_{eff} atomic property with the same cutoff (right). The PCA was applied to 642 TMCs for which ΔE_{1-L} was computed in the IMP data set. The 3d TMCs circles and 4d TMCs squares are overlapping in the right PCA. Metals are colored according to their isovalent pairing: gray for Cr/Mo, green for Mn/Tc, red for Fe/Ru, and blue for Co/Rh, as indicated in inset legend.

We thus add to our original set of RAC heuristic properties the effective nuclear charge, Z_{eff} , which had been shown to be beneficial for increasing transferability in organic molecules.⁸⁰⁻

⁸¹ This property increases the number of feature vector dimensions by $6d+6$ product-based and $3d$ difference-based RACs. For the $d = 3$ cutoff used here, this adds 33 features to our original 152- or 153-dimensional set, and we refer to this set as eRAC-185. The Z_{eff} is identical for isovalent species (e.g., 9 for Co and Rh, 5 for N and P) with distinct principal quantum numbers. As expected, PCA in a subset (i.e., $d = 0$ or 1) of the new Z_{eff} -derived mc-RACs distinguishes TMCs by the metal Z_{eff} in PC1 and by the metal-coordinating ligand atoms in PC2 (Figure 2 and Supporting Information Figure S1). As a result, isovalent 3d and 4d metals (e.g., Co and Rh) will be identical in this feature set, and the full Z_{eff} set of features will order TMCs by increasing d filling and groups isovalent 3d and 4d metals close to each other (Supporting Information Figures S2–S3). Conversely, both PCA and average Euclidean distances over IMP complexes for the full RAC-155 set indicate large differences between isovalent 3d and 4d metal centers and do not reproduce expected trends from the periodic table (Supporting Information Figures S2–S3). Because the new features encode intuitive relationships, we expect that incorporating them into

ML property predictions should be beneficial for learning tasks that span multiple rows in the periodic table.

3. Methods.

3a. Electronic Structure Calculations.

Some of the DFT data used for training in this work was previously published in Ref. ⁷⁹, and all data generation steps followed an established protocol⁷⁰ for DFT training data for octahedral, mononuclear transition-metal complexes⁴⁵, which we reiterate here. DFT geometry optimizations were performed using a development version of TeraChem v1.9.⁸⁶⁻⁸⁷ The B3LYP⁸⁸⁻⁹⁰ global hybrid functional was employed with the LANL2DZ⁹¹ effective core potential for transition metals and the 6-31G* basis⁹² for all other atoms. Singlet calculations were carried out in a spin-restricted formalism, while all other calculations were unrestricted. Level shifting⁹³ was employed to aid self-consistent field convergence with the majority-spin and minority-spin virtual orbitals each shifted by 0.25 Ha. Geometry optimizations were carried out in translation rotation internal coordinates⁹⁴ using the L-BFGS algorithm. Default tolerances of 4.5×10^{-4} hartree/bohr and 10^{-6} hartree were applied in the convergence criteria for the gradient and energy difference between steps, respectively.

Initial structures were generated with molSimplify^{71, 95-96}, which uses OpenBabel⁹⁷⁻⁹⁸ as a backend, and calculations were automated with molSimplify Automatic Design (mAD).^{40, 70} The mAD calculations run for 24 hours of wall time with up to five resubmissions. Geometric criteria⁷⁰ were applied after each resubmission and at tighter thresholds on the final structure (Supporting Information Table S5). We use the same geometric criteria values as in ref. ⁷⁰, which preserve connectivity and penalize excessive asymmetry, except we have tightened the criterion on metal–ligand distance asymmetry for homoleptic complexes (Supporting Information Table

S5). Out of 9,440 initiated $3d$ and $4d$ geometry optimizations, converged structures were obtained for 8,729 TMCs, and 6,480 TMCs satisfied all geometric criteria (Supporting Information Table S6).

As in previous work,^{45, 70-71} criteria based on electronic structure properties were also used to filter the data set. For all open shell (i.e., non-singlet) complexes, calculations with deviations of $\langle S^2 \rangle$ from its expected $S(S+1)$ value by $1 \mu_B^2$ or more were eliminated (196 runs) as were cases where the Mulliken spin on the metal was at least $1 \mu_B$ lower than the expected total spin (292 runs, Supporting Information Table S6). After all filtering steps, 5,992 octahedral $3d$ or $4d$ TMCs were retained for spin-splitting property prediction, but because evaluation of this property requires the convergence of multiple spin states, the final data set sizes were smaller (Supporting Information Table S7). The ΔE_{LD} property was only evaluated for trans or homoleptic complexes with neutral ligands, and filtering steps by the $\langle S^2 \rangle$ and Mulliken metal spin criteria were also applied to these complexes (Supporting Information Table S8).

The retained TMCs were then processed through two additional steps to generate the data sets used in ML model training, a more restrictive procedure than that outlined in Ref.⁷⁹. First, TMCs were paired to construct the IMP and ILP data sets, reducing the candidate TMC set sizes by a factor of two (Supporting Information Tables S3–S4). We then detected cases where the electronic structure was qualitatively distinct between isovalent pairs of complexes, as judged by the metal d -orbital occupations. The occupation of each d orbital was obtained from the NBO v6.0 package³⁸, and a heuristic cutoff of $3 e^-$ for the total difference summed over all d orbitals was used to exclude a pair of calculations (Supporting Information Figure S4). This procedure eliminates a small number (ca. 10–100 for spin-splitting and 250 for ΔE_{LD}) of outliers (Supporting Information Tables S3–S4). The final IMP data sets contain ca. 300–600 pairs of

spin-splitting (i.e., I-L, H-L, or H-I) ΔE values and over 1,000 pairs of ΔE_{LD} values, and the final ILP data sets are a little more than half the size of the IMP sets (Supporting Information Tables S3–S4). The total energies and structures of all TMCs converged in this work along with details of structures eliminated are provided in a .zip file in the Supporting Information.

3b. Machine Learning.

We largely follow a previously developed protocol^{65, 70} for training kernel ridge regression (KRR) models to predict properties in open-shell transition-metal chemistry with some modifications noted. KRR models with a Gaussian kernel were trained on both RAC-155 and eRAC-185 representations and IMP or ILP data using the scikit-learn⁹⁹ software package. The pairs of complexes in the IMP or ILP sets were randomly partitioned into 80% train and 20% validation. The pairs are preserved during the random partitioning, e.g., if an IMP $3d$ complex is in the training set, its isovalent $4d$ counterpart will be as well. All inputs and outputs were normalized to have zero mean and unit variance on the training data.

Two types of models were trained: single-row models that only are trained on a subset of the training data (in practice, from 1–50) from the same row as the learning task, and transfer models that are supplemented with all of the training data from the alternate row. Using the 324-pair of complex IMP set for the $3d$ to $4d$ learning task as an example, models (see Sec. 4) were trained on a subset of the 259-complex 80% $4d$ -only (i.e., single-row models) or this same subset of points along with the 80% $3d$ data (i.e., transfer models). Exhaustive grid search from 10^{-12} to 10^2 with logarithmic spacing was used to select hyperparameters (i.e., kernel width and regularization strength). For the IMP $3d$ to $4d$ example, hyperparameters selected from 10-fold cross-validation errors on $3d$ data produce models with low test set mean unsigned error (MUE) on the in-distribution $3d$ complexes but high MUE on the out-of-distribution $4d$ test set (i.e., the

isovalent pairs to the 20% 3d test set, Supporting Information Figure S5). Thus, we select hyperparameters for each KRR model on the 20% data from the same row as the learning task and hereafter refer to this as the validation MUE, which provides a lower bound of a true unseen test set model error (Supporting Information Figure S5).

Feature selection was employed, as motivated by observations^{65, 70} that it improves KRR model generalization in open-shell transition-metal chemistry. Feature-selected subsets were obtained in a one-shot fashion using LASSO¹⁰⁰ or random forest (RF)¹⁰¹ as in some prior work⁶⁵. Features with an importance greater than 1% were retained from RF. For LASSO feature selection, 5 values for the regularization strength were tested (10^{-2} , 10^{-1} , 10^0 , 10^1 , or 10^2), and all nonzero features were retained from the LASSO model with the lowest validation MUE. The overall feature set (i.e., from LASSO, RF, or the full feature set) that produced the lowest validation MUE was selected for training the KRR model. We report the MUE as the ensemble-average MUE and a credible interval from the ensemble standard deviation. A representative example of the selected hyperparameters, feature selection method, and MUEs is provided in detail in the Supporting Information (Supporting Information Table S9). All other model hyperparameters and feature sets are provided in the Supporting Information .zip file.

4. Results and Discussion.

4a. Correlations of Properties Between Rows.

Because our modified representations are motivated by the assumption that isovalent metals or ligands should exhibit similar properties and structure–property relationships, we first validate this expectation over the IMP and ILP sets. For the isovalent 3d and 4d transition metals in the IMP set, we observe good correlations between the adiabatic gas-phase spin-splitting energies of the first- and second-row metals (Figure 3). This correlation holds somewhat better

($R^2 = 0.9$) for the 2-electron ΔE_{I-L} and 4-electron ΔE_{H-L} than for the 2-electron ΔE_{H-I} ($R^2 = 0.65$) values (Figure 3 and Supporting Information Table S10). As observed in prior work⁷⁹, all $4d$ TMC DFT spin-splitting energies are consistently low-spin shifted with respect to equivalent $3d$ TMCs, especially for strong-field ligands (i.e., with positive $3d$ TMC ΔE values). For the ΔE_{I-L} and ΔE_{H-L} cases where the correlations hold best, the $4d$ TMC ΔE increases by around 1.4 kcal/mol for every 1 kcal/mol increase in the $3d$ TMC (Figure 3 and Supporting Information Table S10).

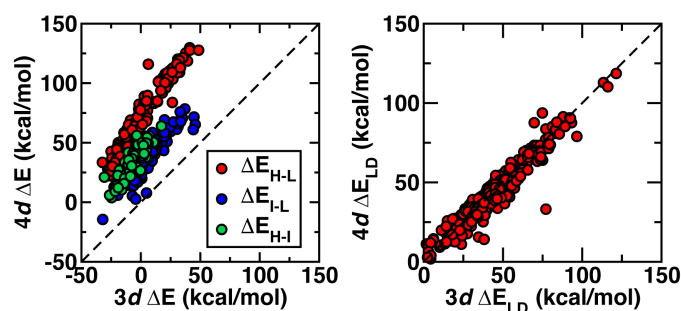


Figure 3. Parity plot for spin-splitting energies, ΔE (left, in kcal/mol) and ligand dissociation energies, ΔE_{LD} (right, in kcal/mol) of Fe/Ru TMCs in the IMP data set. The spin-splitting energy is colored with ΔE_{H-L} in red, ΔE_{I-L} in blue, and ΔE_{H-I} in green, and all data is shown in red at right for ΔE_{LD} . The parity line shown as a dashed black line in both panes.

Despite the apparent good linear correlation over the data set, the MUE of the linear model for predicting $4d$ ΔE_{H-L} from its $3d$ TMC value is still large at around 10 kcal/mol, and the maximum unsigned error is even larger at 45 kcal/mol (Supporting Information Table S10). While MUEs are reduced somewhat for ΔE_{H-I} and ΔE_{I-L} (to ca. 7 kcal/mol), the range of values are also smaller for these properties. Each individual $3d$ or $4d$ metal/oxidation state spans a wide range of ΔE_{H-L} values (ca. 100 kcal/mol), with metal-specific distributions that reflect changes in ligand field strength in our set (i.e., from weak-field halide to strong-field methylisocyanide) for both $3d$ and $4d$ TMCs (Supporting Information Figure S6). When linear models are fit on each individual metal and oxidation state, the MUE of each linear model is somewhat reduced (e.g.,

$\Delta E_{\text{H-L}}$ 4–5 kcal/mol vs 10 kcal/mol for the full set) in part due to the fact that a smaller range of ΔE values is sampled (Supporting Information Figures S7–S9 and Tables S10–S11). Subdividing the data by metal/oxidation state and building individual linear relationships as a strategy for TMC design would nevertheless be challenged by variability in data set sizes (Supporting Information Tables S11–S12). Thus, even though these spin-splitting properties are related for metal pairs in the IMP set, their relationship is not trivial and could be expected to benefit from a flexible ML regression model. A predictive ML model would have the added benefit of not requiring the calculation of one property (e.g., $3d \Delta E_{\text{H-L}}$) to predict the other (e.g., $4d \Delta E_{\text{H-L}}$) that would be required for even a better linear fit.

For the ligand dissociation energy, ΔE_{LD} , introduced in this work, a single linear model obtains good correlation ($R^2 = 0.91$) between $3d$ and $4d$ TMCs over all metals, oxidations, and spin states (Figure 3). The ratio of $4d:3d \Delta E_{\text{LD}}$ values (ca. 0.93) is close to unity but indicates that ligands bind $4d$ TMCs somewhat more weakly than equivalent $3d$ TMCs (Figure 3 and Supporting Information Table S13 and Figure S10). Subdividing ligand dissociation energies by metal/oxidation state or spin provides limited benefit because subset comparisons generally have similar $4d:3d$ ratios and correlation coefficients to the overall set (Supporting Information Tables S13–S14 and Figure S11). Whether overall or in metal/oxidation/spin-state-specific subsets, the MUE of the linear fits is somewhat lower (4–5 kcal/mol) than was observed for spin-splitting energies (Supporting Information Tables S11 and S13).

The ILP set consists of TMCs containing ligands (i.e., six of ten) that vary by isovalent (i.e., $2p$ vs $3p$) changes to the metal-coordinating atom of the ligand. Depending on the metal and oxidation state, the correlation of $2p$ and $3p$ spin-splitting energies ranges from good ($R^2 > 0.9$) to poor ($R^2 < 0.1$), where poorer correlations correspond most typically to unchanged spin-

splitting energies with the ligand substitution and with earlier (i.e., d^3-d^4) transition metals (Supporting Information Figure S12 and Table S15). The influence of the $2p$ to $3p$ isovalent substitution on spin-splitting energies depends on the degree of change in ligand field strength (Figure 4). A consistent trend can be observed over all d^5-d^7 metal centers in either row for the H_2O/H_2S and NH_3/PH_3 substitutions with a good correlation and low standard deviation (Figure 4 and Supporting Information Figure S13 and Table S16).

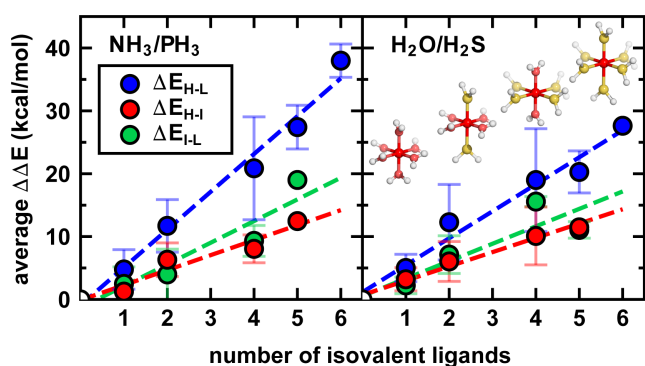


Figure 4. Differences in spin-splitting energies (ΔE_{H-L} in blue, ΔE_{H-I} in red, and ΔE_{I-L} in green, in kcal/mol) with isovalent ligand swaps (NH_3 for PH_3 , left and H_2O for H_2S , right) in the ILP data set averaged over all d^5-d^7 TMCs (i.e., $Mn(II)/Tc(II)$, $Fe(III/II)/Ru(III/II)$, and $Co(III/II)/Rh(III/II)$) where the spin-splitting energy is available and defined. The standard deviation is shown as an error bar along with best-fit lines also fit through (0,0).

Conversely, the limited change in field strength among the halides means these TMCs have a poorer correlation for the substitution (Supporting Information Figure S13 and Table S16). For ΔE_{LD} , trends are less clear, but the $2p$ to $3p$ substitution of two axial ligands (i.e., including the ligand undergoing dissociation) generally decreases the ligand dissociation energy (by 12–16 kcal/mol) for the H_2O/H_2S and NH_3/PH_3 pairs (Supporting Information Tables S17–S18). As with the IMP set, there is a clear structure to the ILP data indicating that properties of $2p$ complexes are related to their $3p$ counterparts, but the relationships depend more strongly on the group identity of the metal-coordinating atom.

We briefly summarize the structure–property relationships uncovered for our learning

tasks to test ML model and representation generalization across the periodic table. For IMP spin-splitting energies, $3d/4d$ relationships are sensitive to the spin states and ligand field strengths being compared, whereas IMP ΔE_{LD} values are comparable across $3d$ and $4d$ TMCs. For ILP spin-splitting energies, $3d/4d$ relationships are dependent on ligand field strength, and ligand dissociation energies are more clearly influenced by the principal quantum number of the dissociated axial ligands. Given the evidence for some relationships between rows of the periodic table, ML model training is expected to benefit from the Z_{eff} heuristics present in eRAC-185.

4b. ML Property Prediction Across the Periodic Table.

Based on the ability of linear models to predict IMP properties as well as some evidence of structure in the ILP data set, we expect that data from one row of the periodic table can be used to inform predictions on isovalent counterparts. To test this hypothesis, we construct a series of KRR models using both RAC-155 and the eRAC-185 representation. We adopt two strategies to test model generalization (see Sec. 3b). While we train all models on a randomly selected and small subset (i.e., from 10–50) of training points from the same row as the 20% validation data, we also train “transfer” models that are supplemented with all available (i.e., the full 80%) training data from the alternate row. To unambiguously identify the training data included in each model, we adopt the notation *data-representation*, where the training *data* is only from the same row (S) as the test (here, also validation) data or transfer (T) data from the alternate row is also included and *representation* is the feature set (i.e., RACs or eRACs) used by the model. For example, a T-eRAC model applied to the $3d$ to $4d$ ΔE_{H-L} learning task will be provided with all available $3d$ ΔE_{H-L} data in the IMP set along with a small number (e.g., 10-50) of randomly-selected $4d$ ΔE_{H-L} points from the IMP set and trained on eRAC-185 and feature-selected subsets (see Sec. 3b).

We first focus on $3d$ to $4d$ prediction of ΔE_{H-L} and ΔE_{LD} in the IMP data set to assess the relative performance of the possible data-representation combinations. Models incorporating data from both rows (i.e., T-(e)RACs) consistently outperform single-row models (i.e., S-(e)RACs), and, simultaneously, eRAC-185-trained models have lower MUEs than models trained with RAC-155 (Figure 5). The MUE is evaluated as the average error from an ensemble of 25 feature-selected models (see Sec. 3b), and observed model performance trends are typically larger in magnitude than the standard deviation of the errors from the ensemble. The benefit of eRAC-185 is most apparent when limited training data (i.e. < 20 points) from the same row as the validation data are used. For example, prediction of ΔE_{LD} from the IMP data set has a substantially lower MUE (by ca. 6.6 kcal/mol) with the T-eRAC model with 20 $4d$ points in the training set than with the S-eRAC model. When we increase the number of $4d$ training points modestly (i.e., to 50), the relative benefit of this additional data from another row is smaller (i.e., the MUE is lower by only ca. 3.5 kcal/mol) but still significant (Supporting Information Table S19).

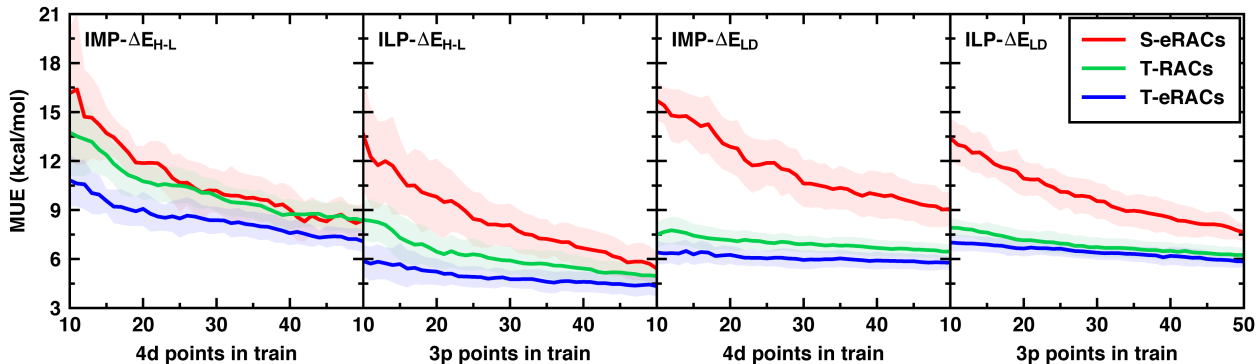


Figure 5. Mean unsigned error (MUE, in kcal/mol) for the prediction of ΔE_{H-L} (left) and ΔE_{LD} (right) properties for the IMP $3d$ to $4d$ learning task and ILP $2p$ to $3p$ learning task with addition of training data as indicated on the x-axis. Transfer-learning models (i.e., that contain all available $3d$ or $2p$ data) with eRAC-185 (blue) and RAC-155 (green) are shown alongside a single-row model (i.e., that only contain $4d$ or $3p$ data) trained on eRAC-185 (red). Shaded areas indicate the standard deviation of the ensemble of 25 models, and the solid line represents the average of this ensemble.

To investigate if this observed maximum benefit of eRAC-185 when few examples from

the same row as the validation data are available is a general phenomenon, we expanded our analysis to models trained to predict ΔE_{I-L} and ΔE_{H-I} with only 20 $4d$ data points. Indeed, we find that transfer models consistently outperform single-row models, and the use of eRAC-185 feature set is synergistic with this benefit (Figure 6). The T-eRAC models consistently achieve the lowest overall MUEs for predicting all three spin-splitting properties, and those trained on eRAC-185 achieve larger reductions in MUE (ca. 2–5 kcal/mol) than equivalent models training using RAC-155 (ca. 1–2 kcal/mol). For predicting ΔE_{LD} , transfer models significantly improve over single-row models (by ca. 6 kcal/mol), but this improvement is observed for both RAC-155 and eRAC-185 representations (Supporting Information Table S19). We attribute the difference in ΔE_{LD} model errors to the observed lack of dependence on the principal quantum number of the metal for this property (see Sec. 4a).

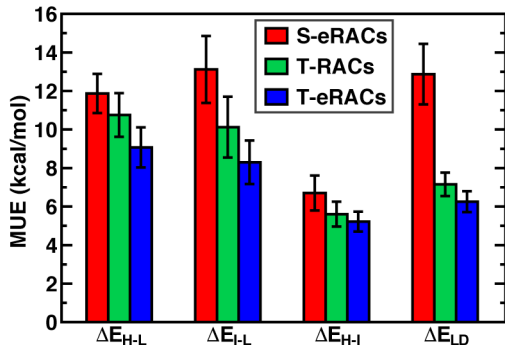


Figure 6. Mean unsigned error (MUE, in kcal/mol) for the prediction of $4d$ TMC properties with only 20 $4d$ data points with eRAC-185 (red) or by including $3d$ data with 20 $4d$ data points and using either the RAC-155 (green) or eRAC-185 (blue) on the IMP data set. The colored bars represent the average from an ensemble of 25 feature-selected KRR models, and the error bars are the standard deviation of the ensemble.

To probe the source of benefit of the inclusion of the first 20 inter-row data points, we developed an additional ML model training procedure in which we grouped inter-row data by metal in order to preferentially add one metal at a time to the training set. When the training data includes only a single $4d$ metal (i.e. Mo, Tc, Ru, or Rh) for ΔE_{I-L} , no improvement in the model

is observed (Supporting Information Figure S14). Rather than reducing MUEs with more data, the MUEs are instead high and constant at approximately 15 kcal/mol when one to 15 training points of this type are added (Supporting Information Table S20). If data points are added from multiple additional *4d* metals, performance instead improves significantly. In this case, MUEs for predicting ΔE_{I-L} reduce to ca. 11 kcal/mol when training data includes two *4d* metals (Supporting Information Table S20). After adding fewer than 20 points, the T-eRAC model with knowledge of two *4d* metals alongside all *3d* metals outperforms the S-eRAC model (MUE: 13 kcal/mol) that was trained on 20 random points that included all *4d* metals (Figure 6 and Supporting Information Figure S15). The MUE is reduced further when a third *4d* metal (i.e., to 7.8 kcal/mol) and all *4d* metals (i.e., to 6.2 kcal/mol) are included in the training set (Supporting Information Table S20). Thus, we expect that inter-row models perform best when examples of each new metal type are included in the training data by giving the model balanced information about the relationship among all groups of the periodic table studied in the validation set. The significance of the identified sample size of 20 inter-row data points maximizing benefit in transfer models is likely attributable to reaching a sample that includes sufficient diversity of isovalent metals or ligands. This result is non-trivial because at such small set sizes, the model has information about all metals but not in combination with ligands and thus must infer the cooperativity of metal and ligand field effects.

Returning to the eRAC-185 representation, we tested whether its observed benefit in the IMP data set *3d* to *4d* learning task is general to both the reverse learning task (i.e., *4d* to *3d* IMP) as well as to changes in ligand chemistry (i.e., *2p* to *3p* ILP and *3p* to *2p* ILP). Across all of these learning tasks, a combination of transfer models and eRAC-185 reduces validation MUEs for most properties, with results and improvements comparable to those observed for the IMP *3d*

to $4d$ learning task (Supporting Information Figure S15). In all learning tasks and properties compared, ILP $2p$ to $3p$ and $3p$ to $2p$ ΔE_{H-I} are the only cases where RAC-155-trained models outperform eRAC-185, but these difference are small (0.3 kcal/mol) and within the standard deviation (0.6 kcal/mol) of the 25-model ensembles (Supporting Information Table S21). As in the IMP data set, the benefit of inter-row, transfer models trained to predict ΔE_{LD} in the ILP set (ca. 6 kcal/mol) is observed to be independent of the representation (i.e., RAC-155 or eRAC-185) chosen. For spin-splitting energy prediction in the ILP set, we again observe that eRAC-185 improves inter-row models, with T-eRAC models outperforming single-row models by a slightly larger margin (ca. 2–6 kcal/mol) than T-RAC models (ca. 2–4 kcal/mol). Taken together, we conclude that the use of eRAC-185 in combination with a transfer model trained on a small set of examples from the new learning task provides a near-universal benefit and never significantly degrades the accuracy in comparison to a standard ML model.

4c. Feature Analysis Reveals Learned Chemical Trends.

To investigate the source of the improved performance observed when using eRAC-185, we evaluate the averaged, down-selected feature space. For each model in the ensemble, features are selected independently (i.e., from one-shot LASSO or random forest 1% cutoff, see Sec. 3b), so this analysis is on the normalized feature contribution is averaged over the KRR models in the ensemble. Features containing the Z_{eff} atomic property are frequently selected in inter-row models for predicting both spin-splitting energies and ΔE_{LD} (see Supporting Information .zip file for all features and models). For $3d$ to $4d$ prediction of ΔE_{I-L} (i.e., on the IMP set), Z_{eff} eRACs involving the metal center, atoms one bond-path away from the metal, and atoms two bond-paths away from the metal are all selected (Figure 7). This suggests that the T-eRAC models achieve performance improvements by positioning both metals and ligands closer to their inter-row

counterparts in the feature space than standard RACs. In contrast, for $3d$ to $4d$ prediction of ΔE_{LD} , Z_{eff} features involving the metal are rarely selected (Figure 7). This analysis mirrors our observation that the expanded representation did not lead to significant improvements for a ΔE_{LD} inter-row, transfer model (see Sec. 4b) due to the relative lack of dependence of the ligand dissociation on the principal quantum number of the metal.

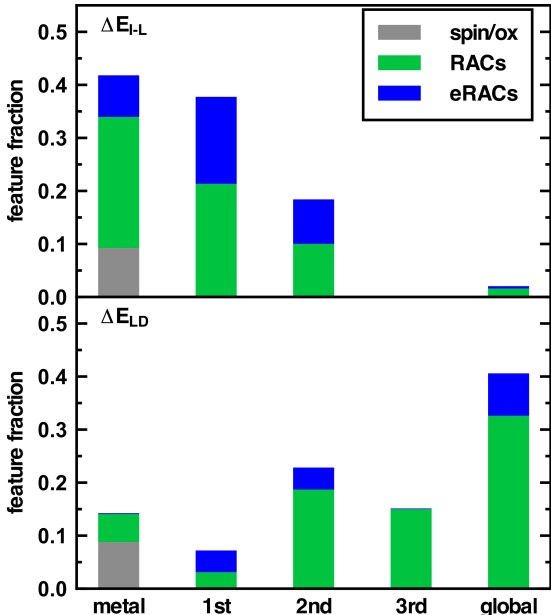


Figure 7. Feature fraction grouped by the most metal-distant atom in the feature (i.e., metal, 1st, 2nd, 3rd, or global) and shown as a stacked bar plot. Colors within each feature fraction correspond to whether the features are obtained from RACs (green), the eRAC-specific Z_{eff} features (blue), or features encoding the metal center's spin and oxidation state (gray). The selected features are obtained from their normalized weight in an ensemble of 25 models (i.e., T-RACs or T-eRACs) trained to predict $4d$ properties using $3d$ data along with 20 $4d$ data points.

We analyzed other learning tasks (i.e., beyond $3d$ to $4d$ learning of ΔE_{I-L} and ΔE_{LD}) to confirm that the benefit of using eRAC-185 was due to the presence of Z_{eff} features in feature-selected subsets. Prior to feature selection, the Z_{eff} features comprise 18% of the initial eRAC-185 set, and they are frequently retained after feature selection regardless of the learning task or property (Supporting Information Figure S16). For the ΔE_{I-L} and ΔE_{H-I} properties where Z_{eff} -based features were most beneficial in model performance (see Sec. 4b), Z_{eff} contributions are

enriched (to ca. 23% of features) after feature selection. For ΔE_{LD} and ΔE_{H-I} , cases where Z_{eff} -based features provided less benefit, they are retained at a comparable frequency (ca. 18% of the down-selected features) to others in the set, confirming that these features are neither particularly detrimental nor beneficial (Supporting Information Table S22).

As in previous work^{38, 65, 70, 72} we also analyzed the selected features to reveal qualitative chemical trends in the data set. We select ΔE_{I-L} 3d to 4d learning as a representative property for spin-splitting energy trends (Supporting Information Figure S16). Features retained by models trained on ΔE_{I-L} are strongly metal-local, with 80% corresponding to the metal or its immediate coordinating atoms. Since this result recapitulates observations from prior work⁶⁵ that emphasized the metal-local nature of spin-splitting energy prediction, the tailored representation preserves known trends (Figure 7 and Supporting Information Table S23). We next analyze the features selected for predicting ΔE_{LD} , which is a property for which we had not previously trained ML models. In this case, the retained features are 79% distal (i.e., with information from atoms two or more bonds away) from the metal (Figure 7 and Supporting Information Table S23). The high weight of ligand-based features and more global information is consistent with our observations of reduced dependence on the principal quantum number of the metal for ΔE_{LD} prediction (Figure 3). Thus, feature analysis suggests it is possible to design ligand binding strength (e.g., for catalysis) in a metal-row-independent fashion (e.g., predicting 4d properties from data obtained on 3d TMCs). Conversely, because spin state is dictated both by the metal center and only the immediate coordinating atoms of the ligand, inter-row transfer models trained on eRACs and minimal but chemically diverse TMCs⁷⁴ should enable accelerated prediction of 4d TMC spin-splitting in cases where only 3d TMC data is available.

Because the property prediction obtained from a KRR model depends on a combination

of feature-space distances and the kernel width, the relative distances between TMCs in a representation are critical for understanding model performance. We thus quantify the Euclidean norm distance between complexes with differing metals in feature-selected subspaces that have been averaged and normalized over the 25-model ensembles used for property prediction. In the features selected in T-RAC models, these Euclidean distances do not represent what we would expect from the arrangement of elements on the periodic table (Supporting Information Table S24). For example, in the $3d$ to $4d$ prediction of ΔE_{I-L} , Cr is positioned closer to Fe and Co in the feature space than it is to the more chemically similar Mn. Furthermore, Cr is comparatively distant to all of the $4d$ metals, artificially reducing its influence on predicting their properties (Figure 8). In contrast, the features retained in T-eRAC models rearrange the feature space to more closely match intuition from the periodic table, with Cr in closest proximity to Mn and Mn in closest proximity to Cr and Fe. The $3d$ and $4d$ metal pairs are also shifted closer together in T-eRAC models. For example, $3d$ Cr is closer to isovalent $4d$ Mo than to a dissimilar $3d$ metal such as Co (Figure 8). The rearrangement of the feature space is observed for other metals, with $3d/4d$ pairs shifted an average of 13% closer in T-eRAC models in comparison to equivalent T-RAC models (Supporting Information Table S24). These results suggest that the reduced prediction error when using eRAC-185 (see Sec. 4b) can be attributed to this representation encoding chemical trends more efficiently.

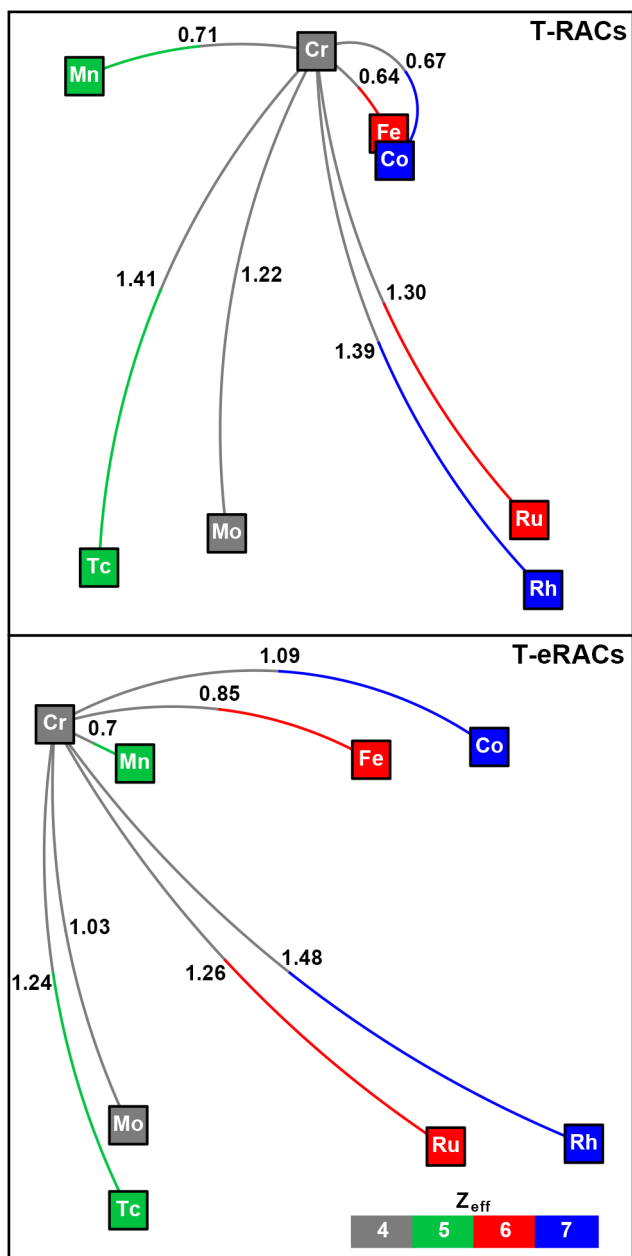


Figure 8. Distribution of average, normalized distances of TMCs with the feature-selected subsets of T-RACs (top) or T-eRACs (bottom) from the ensemble of 25 KRR models trained to predict $4d \Delta E_{I-L}$ based on $3d$ data and 20 $4d$ examples (i.e., transfer models) visualized in a two-dimensional projection of the feature space. The average distances between Cr TMCs and TMCs with other metal centers are labeled. Elements are colored by their Z_{eff} values to highlight isovalent $3d/4d$ pairs according to inset legend. The feature-space distances were normalized such that the average distance between any two TMCs is equal to one, and the weight of features selected from the ensemble were also normalized.

5. Conclusions.

Since chemical relationships between neighboring elements in the periodic table can be expected, efficient strategies for ML-driven discovery should leverage representations that preserve these similarities. After confirming the strong inter-row structure–property relationships for spin-splitting energies and ligand dissociation in isovalent $3d/4d$ metals and $2p/3p$ ligands in large sets (ca. 1000 pairs) of data, we identified a strategy for increasing ML model transferability. We introduced eRAC-185, a tailored representation that blends together the monotonically increasing nuclear charge with the periodic in nature effective nuclear charge heuristics. We showed how the addition of the Z_{eff} heuristic property in eRACs altered feature-space distances to encode a more intuitive degree of similarity among isovalent elements essential for kernel-based ML models.

Next, we demonstrated the synergistic value of eRACs alongside a transfer learning approach to leverage inter-row data in sets containing isovalent metals or ligand-coordinating atoms in transition-metal chemistry. To assess the potential improved performance of eRAC-185, we trained KRR models using data from either only the same row as the prediction task or both rows of the periodic table. While including data from the alternate row always reduced prediction errors, the eRAC-185 model errors were most substantially improved in the limit of very low data (ca. 20 points). The model error improvement was strongest when the relationship being learned deviated most from parity. This highlights how transferable representations will be essential to improve ML model generalization from one row of the periodic table to another especially when carrying out chemical discovery where limited prior knowledge is available.

To identify differences in models trained on eRAC-185, we analyzed the distance and heuristic atomic properties retained during feature selection. Feature-space distances of TMCs grouped and averaged by metals confirmed that eRAC-185 subsets faithfully represented trends

expected from the periodic table, causing elements from the same or adjacent group to influence KRR predictions most strongly. These representations, models, and approach can be leveraged to accelerate the discovery of earth-abundant catalysts or materials from known materials featuring scarcer elements. We expect our strategies for inter-row design and expanding transferability to be broadly useful to other materials challenges across the periodic table.

ASSOCIATED CONTENT

Supporting Information.

Spin multiplicity definitions; subset of combinations studied for cis TMCs; statistics for filtering and pairing structures as well as 3d/4d comparisons to obtain properties; PCA of RAC and eRAC representations; comparison of Euclidean distance between metals by featurization type; geometry metrics used for geometric filtering; number of compounds failed at each filtering step with reasons; details of NBO d orbital check elimination; cross-validation heat maps for hyperparameter selection; KRR model hyperparameters by model number; linear models for inter-row property prediction for the IMP dataset, overall and broken down by metal; histograms of property distributions for spin splitting energy; inter-row parity plots for properties by metal and oxidation state; ligand dissociation energy distribution broken down by metal and oxidation state; frequencies of ligand dissociation energy by metal, oxidation, and spin state in the IMP and ILP data sets; parity plots for spin splitting energy in the IMP set; changes in property by ligand mixing for three spin splitting energy properties; linear models for spin splitting energies in ILP dataset split by metal, oxidation state, and type of spin splitting energy; change in spin splitting energy as a function of ligand mixing in the ILP data set; quantification of ligand substitution in ILP dataset quantified by ligand type; differences in ligand dissociation energy for compounds that vary only in equatorial ligands or only in axial ligands; quantification of test set errors for KRR model ensembles for various inter-row learning tasks; model performance by ordered metal addition for 4d metals; quantification of errors with ordered metal addition of 4d metals; mean unsigned errors for various inter-row learning schemes over the IMP and ILP data sets; stacked bar charts for feature character for different properties obtained during each scheme of inter-row learning, and tabulation of corresponding feature character by property and bond depth; quantification of feature space distances for feature selected subspaces of 3d/4d models in the IMP data set (PDF)

Structures and total energies of all 3d and 4d TMCs studied in this work; reasons complexes were not included in the dataset; spin splitting values for all pairs of 3d/4d TMCs; ligand dissociation energies for 3d/4d TMCs; total energies of all TMCs; KRR model performance and selected features and ensemble quantification (ZIP)

This material is available free of charge via the Internet at <http://pubs.acs.org>.

AUTHOR INFORMATION

Corresponding Author

*email: hjkulik@mit.edu phone: 617-253-4584

Notes

The authors declare no competing financial interest.

ACKNOWLEDGMENT

The authors acknowledge initial partial support in data generation steps and machine learning representation development (for A.N.) by the United States Department of Energy under grant number DE-SC0012702. The work was also supported by the Office of Naval Research under grant numbers N00014-17-1-2956 and N00014-18-1-2434 (D.H. and J.P.J.) as well as N00014-20-1-2150 (C.D., D.H., and N.A.) as well as DARPA grant D18AP00039 (for N.A., C.D., and A.N). Ligand dissociation studies were supported by the National Science Foundation under grant number CBET-1704266 (for A.N.). A.N. was partially supported by a National Science Foundation Graduate Research Fellowship under Grant #1122374. H.J.K. holds a Career Award at the Scientific Interface from the Burroughs Wellcome Fund and an AAAS Marion Milligan Mason Award, which supported this work. This work was carried out in part using computational resources from the Extreme Science and Engineering Discovery Environment (XSEDE), which is supported by National Science Foundation grant number ACI-1548562. The authors thank Adam H. Steeves for providing a critical reading of the manuscript.

References

1. Curtarolo, S.; Hart, G. L. W.; Nardelli, M. B.; Mingo, N.; Sanvito, S.; Levy, O., The High-Throughput Highway to Computational Materials Design. *Nat Mater* **2013**, *12*, 191-201.

2. Jain, A.; Ong, S. P.; Hautier, G.; Chen, W.; Richards, W. D.; Dacek, S.; Cholia, S.; Gunter, D.; Skinner, D.; Ceder, G.; Persson, K. A., Commentary: The Materials Project: A Materials Genome Approach to Accelerating Materials Innovation. *APL Mater.* **2013**, *1*, 011002.
3. Meredig, B.; Agrawal, A.; Kirklin, S.; Saal, J. E.; Doak, J. W.; Thompson, A.; Zhang, K.; Choudhary, A.; Wolverton, C., Combinatorial Screening for New Materials in Unconstrained Composition Space with Machine Learning. *Phys. Rev. B* **2014**, *89*, 094104.
4. Dral, P. O., Quantum Chemistry in the Age of Machine Learning. *J. Phys. Chem. Lett.* **2020**, *11*, 2336-2347.
5. Janet, J. P.; Duan, C.; Nandy, A.; Liu, F.; Kulik, H. J., Navigating Transition-Metal Chemical Space: Artificial Intelligence for First-Principles Design. *Acc. Chem. Res.* **2021**, *54*, 532-545.
6. Butler, K. T.; Davies, D. W.; Cartwright, H.; Isayev, O.; Walsh, A., Machine Learning for Molecular and Materials Science. *Nature* **2018**, *559*, 547-555.
7. Mater, A. C.; Coote, M. L., Deep Learning in Chemistry. *J. Chem. Inf. Model.* **2019**, *59*, 2545-2559.
8. Goldsmith, B. R.; Esterhuizen, J.; Liu, J. X.; Bartel, C. J.; Sutton, C., Machine Learning for Heterogeneous Catalyst Design and Discovery. *AIChE J.* **2018**, *64*, 2311-2323.
9. Janet, J. P.; Ramesh, S.; Duan, C.; Kulik, H. J., Accurate Multiobjective Design in a Space of Millions of Transition Metal Complexes with Neural-Network-Driven Efficient Global Optimization. *ACS Cent. Sci.* **2020**, *6*, 513-524.
10. Herbol, H. C.; Hu, W.; Frazier, P.; Clancy, P.; Poloczek, M., Efficient Search of Compositional Space for Hybrid Organic–Inorganic Perovskites via Bayesian Optimization. *npj Comput. Mater.* **2018**, *4*, 51.
11. Hernández-Lobato, J. M.; Requeima, J.; Pyzer-Knapp, E. O.; Aspuru-Guzik, A. In *Parallel and Distributed Thompson Sampling for Large-Scale Accelerated Exploration of Chemical Space*, Proceedings of the 34th International Conference on Machine Learning, Proceedings of Machine Learning Research, Doina, P.; Yee Whye, T., Eds. PMLR: Proceedings of Machine Learning Research, 2017; pp 1470-1479.
12. Tran, K.; Ulissi, Z. W., Active Learning across Intermetallics to Guide Discovery of Electrocatalysts for CO₂ Reduction and H₂ Evolution. *Nat. Catal.* **2018**, *1*, 696-703.
13. Kerr, W. J.; Knox, G. J.; Reid, M.; Tuttle, T., Catalyst Design in C–H Activation: A Case Study in the Use of Binding Free Energies to Rationalise Intramolecular Directing Group Selectivity in Iridium Catalysis. *Chem. Sci.* **2021**, *12*, 6747-6755.
14. Duan, L.; Bozoglian, F.; Mandal, S.; Stewart, B.; Privalov, T.; Llobet, A.; Sun, L., A Molecular Ruthenium Catalyst with Water-Oxidation Activity Comparable to That of Photosystem II. *Nat. Chem.* **2012**, *4*, 418-423.
15. Zadrozny, J. M.; Atanasov, M.; Bryan, A. M.; Lin, C.-Y.; Rekker, B. D.; Power, P. P.; Neese, F.; Long, J. R., Slow Magnetization Dynamics in a Series of Two-Coordinate Iron(II) Complexes. *Chem. Sci.* **2013**, *4*, 125-138.
16. Bunting, P. C.; Atanasov, M.; Damgaard-Møller, E.; Perfetti, M.; Crassee, I.; Orlita, M.; Overgaard, J.; van Slageren, J.; Neese, F.; Long, J. R., A Linear Cobalt(II) Complex with Maximal Orbital Angular Momentum from a Non-Aufbau Ground State. *Science* **2018**, *362*.
17. Vollmer, I.; Ould-Chikh, S.; Aguilar-Tapia, A.; Li, G.; Pidko, E.; Hazemann, J.-L.; Kapteijn, F.; Gascon, J., Activity Descriptors Derived from Comparison of Mo and Fe as Active Metal for Methane Conversion to Aromatics. *J. Am. Chem. Soc.* **2019**, *141*, 18814-18824.

18. Bullock, R. M.; Chen, J. G.; Gagliardi, L.; Chirik, P. J.; Farha, O. K.; Hendon, C. H.; Jones, C. W.; Keith, J. A.; Klosin, J.; Minter, S. D., Using Nature's Blueprint to Expand Catalysis with Earth-Abundant Metals. *Science* **2020**, 369.
19. Chirik, P.; Morris, R., Getting Down to Earth: The Renaissance of Catalysis with Abundant Metals. *Acc. Chem. Res.* **2015**, 48, 2495-2495.
20. Filonenko, G. A.; van Putten, R.; Hensen, E. J. M.; Pidko, E. A., Catalytic (De)Hydrogenation Promoted by Non-Precious Metals—Co, Fe and Mn: Recent Advances in an Emerging Field. *Chem. Soc. Rev.* **2018**, 47, 1459-1483.
21. Zuo, W.; Lough, A. J.; Li, Y. F.; Morris, R. H., Amine (Imine) Diphosphine Iron Catalysts for Asymmetric Transfer Hydrogenation of Ketones and Imines. *Science* **2013**, 342, 1080-1083.
22. Friedfeld, M. R.; Zhong, H.; Ruck, R. T.; Shevlin, M.; Chirik, P. J., Cobalt-Catalyzed Asymmetric Hydrogenation of Enamides Enabled by Single-Electron Reduction. *Science* **2018**, 360, 888-893.
23. Klug, C. M.; Cardenas, A. J. P.; Bullock, R. M.; O'Hagan, M.; Wiedner, E. S., Reversing the Tradeoff between Rate and Overpotential in Molecular Electrocatalysts for H₂ Production. *ACS Catal.* **2018**, 8, 3286-3296.
24. Le Goff, A.; Artero, V.; Josselme, B.; Tran, P. D.; Guillet, N.; Métayé, R.; Fihri, A.; Palacin, S.; Fontecave, M., From Hydrogenases to Noble Metal-Free Catalytic Nanomaterials for H₂ Production and Uptake. *Science* **2009**, 326, 1384-1387.
25. Huan, T. N.; Jane, R. T.; Benayad, A.; Guetaz, L.; Tran, P. D.; Artero, V., Bio-Inspired Noble Metal-Free Nanomaterials Approaching Platinum Performances for H₂ Evolution and Uptake. *Energy Environ. Sci.* **2016**, 9, 940-947.
26. Azcarate, I.; Costentin, C.; Robert, M.; Savéant, J.-M., Through-Space Charge Interaction Substituent Effects in Molecular Catalysis Leading to the Design of the Most Efficient Catalyst of CO₂-to-CO Electrochemical Conversion. *J. Am. Chem. Soc.* **2016**, 138, 16639-16644.
27. Martin, D. J.; Mercado, B. Q.; Mayer, J. M., Combining Scaling Relationships Overcomes Rate Versus Overpotential Trade-Offs in O₂ Molecular Electrocatalysis. *Sci. Adv.* **2020**, 6, eaaz3318.
28. Bartók, A. P.; De, S.; Poelking, C.; Bernstein, N.; Kermode, J. R.; Csányi, G.; Ceriotti, M., Machine Learning Unifies the Modeling of Materials and Molecules. *Sci. Adv.* **2017**, 3, e1701816.
29. Chen, C.; Ye, W.; Zuo, Y.; Zheng, C.; Ong, S. P., Graph Networks as a Universal Machine Learning Framework for Molecules and Crystals. *Chem. Mater.* **2019**, 31, 3564-3572.
30. Faber, F. A.; Christensen, A. S.; Huang, B.; Von Lilienfeld, O. A., Alchemical and Structural Distribution Based Representation for Universal Quantum Machine Learning. *J. Chem. Phys.* **2018**, 148, 241717.
31. Von Lilienfeld, O. A., Quantum Machine Learning in Chemical Compound Space. *Angew. Chem., Int. Ed.* **2018**, 57, 4164-4169.
32. Ramakrishnan, R.; Dral, P. O.; Rupp, M.; Von Lilienfeld, O. A., Quantum Chemistry Structures and Properties of 134 Kilo Molecules. *Sci. Data* **2014**, 1, 140022.
33. Zheng, X.; Zheng, P.; Zhang, R.-Z., Machine Learning Material Properties from the Periodic Table Using Convolutional Neural Networks. *Chem. Sci.* **2018**, 9, 8426-8432.
34. Vogiatzis, K. D.; Polynski, M. V.; Kirkland, J. K.; Townsend, J.; Hashemi, A.; Liu, C.; Pidko, E. A., Computational Approach to Molecular Catalysis by 3d Transition Metals: Challenges and Opportunities. *Chem. Rev.* **2018**, 119, 2453-2523.

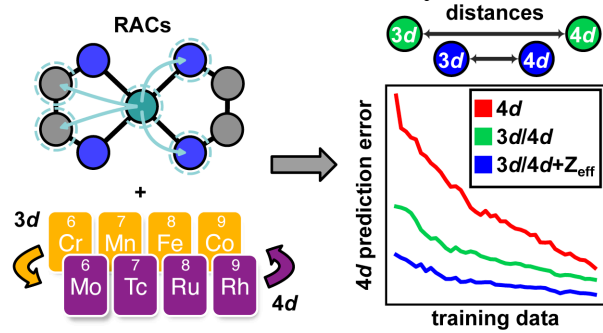
35. Friederich, P.; dos Passos Gomes, G.; De Bin, R.; Aspuru-Guzik, A.; Balcells, D., Machine Learning Dihydrogen Activation in the Chemical Space Surrounding Vaska's Complex. *Chem. Sci.* **2020**, *11*, 4584-4601.
36. Meyer, B.; Sawatlon, B.; Heinen, S.; von Lilienfeld, O. A.; Corminboeuf, C., Machine Learning Meets Volcano Plots: Computational Discovery of Cross-Coupling Catalysts. *Chem. Sci.* **2018**, *9*, 7069-7077.
37. Cordova, M.; Wodrich, M. D.; Meyer, B.; Sawatlon, B.; Corminboeuf, C., Data-Driven Advancement of Homogeneous Nickel Catalyst Activity for Aryl Ether Cleavage. *ACS Catal.* **2020**, *10*, 7021-7031.
38. Nandy, A.; Zhu, J.; Janet, J. P.; Duan, C.; Getman, R. B.; Kulik, H. J., Machine Learning Accelerates the Discovery of Design Rules and Exceptions in Stable Metal- Oxo Intermediate Formation. *ACS Catal.* **2019**, *9*, 8243-8255.
39. Maley, Steven M.; Kwon, D.-H.; Rollins, N.; Stanley, J. C.; Sydora, O. L.; Bischof, S. M.; Ess, D. H., Quantum-Mechanical Transition-State Model Combined with Machine Learning Provides Catalyst Design Features for Selective Cr Olefin Oligomerization. *Chem. Sci.* **2020**, *11*, 9665-9674.
40. Janet, J. P.; Chan, L.; Kulik, H. J., Accelerating Chemical Discovery with Machine Learning: Simulated Evolution of Spin Crossover Complexes with an Artificial Neural Network. *J. Phys. Chem. Lett.* **2018**, *9*, 1064-1071.
41. Moosavi, S. M.; Nandy, A.; Jablonka, K. M.; Ongari, D.; Janet, J. P.; Boyd, P. G.; Lee, Y.; Smit, B.; Kulik, H. J., Understanding the Diversity of the Metal-Organic Frameworks Ecosystems. *Nat. Commun.* **2020**, *11*, 4068.
42. Fanourgakis, G. S.; Gkagkas, K.; Tylanakis, E.; Froudakis, G. E., A Universal Machine Learning Algorithm for Large-Scale Screening of Materials. *J. Am. Chem. Soc.* **2020**, *142*, 3814-3822.
43. Yao, Z.; Sánchez-Lengeling, B.; Bobbitt, N. S.; Bucior, B. J.; Kumar, S. G. H.; Collins, S. P.; Burns, T.; Woo, T. K.; Farha, O. K.; Snurr, R. Q.; Aspuru-Guzik, A., Inverse Design of Nanoporous Crystalline Reticular Materials with Deep Generative Models. *Nat. Mach. Intell.* **2021**, *3*, 76-86.
44. Eckhoff, M.; Lausch, K. N.; Blöchl, P. E.; Behler, J., Predicting Oxidation and Spin States by High-Dimensional Neural Networks: Applications to Lithium Manganese Oxide Spinels. *J. Chem. Phys.* **2020**, *153*, 164107.
45. Duan, C.; Janet, J. P.; Liu, F.; Nandy, A.; Kulik, H. J., Learning from Failure: Predicting Electronic Structure Calculation Outcomes with Machine Learning Models. *J. Chem. Theory Comput.* **2019**, *15*, 2331-2345.
46. Husch, T.; Sun, J.; Cheng, L.; Lee, S. J. R.; Miller, T. F., Improved Accuracy and Transferability of Molecular-Orbital-Based Machine Learning: Organics, Transition-Metal Complexes, Non-Covalent Interactions, and Transition States. *J. Chem. Phys.* **2021**, *154*, 064108.
47. Wodrich, M. D.; Sawatlon, B.; Busch, M.; Corminboeuf, C., The Genesis of Molecular Volcano Plots. *Acc. Chem. Res.* **2021**, *54*, 1107-1117.
48. Welborn, M.; Cheng, L.; Miller III, T. F., Transferability in Machine Learning for Electronic Structure via the Molecular Orbital Basis. *J. Chem. Theory Comput.* **2018**, *14*, 4772-4779.

49. Chang, A. M.; Freeze, J. G.; Batista, V. S., Hammett Neural Networks: Prediction of Frontier Orbital Energies of Tungsten–Benzylidyne Photoredox Complexes. *Chem. Sci.* **2019**, *10*, 6844-6854.
50. Bucior, B. J.; Rosen, A. S.; Haranczyk, M.; Yao, Z.; Ziebel, M. E.; Farha, O. K.; Hupp, J. T.; Siepmann, J. I.; Aspuru-Guzik, A.; Snurr, R. Q., Identification Schemes for Metal–Organic Frameworks to Enable Rapid Search and Cheminformatics Analysis. *Cryst. Growth Des.* **2019**, *19*, 6682-6697.
51. Mikami, K., Interactive-Quantum-Chemical-Descriptors Enabling Accurate Prediction of an Activation Energy through Machine Learning. *Polymer* **2020**, *203*, 122738.
52. Foscatto, M.; Jensen, V. R., Automated in Silico Design of Homogeneous Catalysts. *ACS Catal.* **2020**, *10*, 2354-2377.
53. Durand, D. J.; Fey, N., Computational Ligand Descriptors for Catalyst Design. *Chem. Rev.* **2019**, *119*, 6561-6594.
54. Weymuth, T.; Reiher, M., Inverse Quantum Chemistry: Concepts and Strategies for Rational Compound Design. *Int. J. Quantum Chem.* **2014**, *114*, 823-837.
55. Freeze, J. G.; Kelly, H. R.; Batista, V. S., Search for Catalysts by Inverse Design: Artificial Intelligence, Mountain Climbers, and Alchemists. *Chem. Rev.* **2019**, *119*, 6595-6612.
56. Xiao, D.; Martini, L. A.; Snoeberger Iii, R. C.; Crabtree, R. H.; Batista, V. S., Inverse Design and Synthesis of Acac-Coumarin Anchors for Robust TiO₂ Sensitization. *J. Am. Chem. Soc.* **2011**, *133*, 9014-9022.
57. Chang, A. M.; Rudshiteyn, B.; Warnke, I.; Batista, V. S., Inverse Design of a Catalyst for Aqueous CO/CO₂ Conversion Informed by the Niⁱⁱⁱ–Iminothiolate Complex. *Inorg. Chem.* **2018**, *57*, 15474-15480.
58. Bergeler, M.; Simm, G. N.; Proppe, J.; Reiher, M., Heuristics-Guided Exploration of Reaction Mechanisms. *J. Chem. Theory Comput.* **2015**, *11*, 5712-5722.
59. Fernandez, M.; Trefiak, N. R.; Woo, T. K., Atomic Property Weighted Radial Distribution Functions Descriptors of Metal–Organic Frameworks for the Prediction of Gas Uptake Capacity. *J. Phys. Chem. C* **2013**, *117*, 14095-14105.
60. Rupp, M.; Tkatchenko, A.; Muller, K. R.; von Lilienfeld, O. A., Fast and Accurate Modeling of Molecular Atomization Energies with Machine Learning. *Phys. Rev. Lett.* **2012**, *108*, 058301.
61. Bartók, A. P.; Kondor, R.; Csányi, G., On Representing Chemical Environments. *Phys. Rev. B* **2013**, *87*, 184115.
62. Hansen, K.; Biegler, F.; Ramakrishnan, R.; Pronobis, W.; Von Lilienfeld, O. A.; Müller, K.-R.; Tkatchenko, A., Machine Learning Predictions of Molecular Properties: Accurate Many-Body Potentials and Nonlocality in Chemical Space. *J. Phys. Chem. Lett.* **2015**, *6*, 2326-2331.
63. Behler, J.; Parrinello, M., Generalized Neural-Network Representation of High-Dimensional Potential-Energy Surfaces. *Phys. Rev. Lett.* **2007**, *98*, 146401.
64. Duvenaud, D.; Maclaurin, D.; Aguilera-Iparraguirre, J.; Gómez-Bombarelli, R.; Hirzel, T.; Aspuru-Guzik, A.; Adams, R. P., Convolutional Networks on Graphs for Learning Molecular Fingerprints. *arXiv preprint arXiv:1509.09292* **2015**.
65. Janet, J. P.; Kulik, H. J., Resolving Transition Metal Chemical Space: Feature Selection for Machine Learning and Structure–Property Relationships. *J. Phys. Chem. A* **2017**, *121*, 8939-8954.
66. Burello, E.; Rothenberg, G., Topological Mapping of Bidentate Ligands: A Fast Approach for Screening Homogeneous Catalysts. *Adv. Synth. Catal.* **2005**, *347*, 1969-1977.

67. Moreau, G.; Broto, P., The Autocorrelation of a Topological Structure: A New Molecular Descriptor. *Nouv. J. Chim.* **1980**, *4*, 359-360.
68. Virshup, A. M.; Contreras-García, J.; Wipf, P.; Yang, W.; Beratan, D. N., Stochastic Voyages into Uncharted Chemical Space Produce a Representative Library of All Possible Drug-Like Compounds. *J. Am. Chem. Soc.* **2013**, *135*, 7296-7303.
69. Janet, J. P.; Liu, F.; Nandy, A.; Duan, C.; Yang, T.; Lin, S.; Kulik, H. J., Designing in the Face of Uncertainty: Exploiting Electronic Structure and Machine Learning Models for Discovery in Inorganic Chemistry. *Inorg. Chem.* **2019**, *58*, 10592-10606.
70. Nandy, A.; Duan, C.; Janet, J. P.; Gugler, S.; Kulik, H. J., Strategies and Software for Machine Learning Accelerated Discovery in Transition Metal Chemistry. *Ind. Eng. Chem. Res.* **2018**, *57*, 13973-13986.
71. Janet, J. P.; Duan, C.; Yang, T.; Nandy, A.; Kulik, H. J., A Quantitative Uncertainty Metric Controls Error in Neural Network-Driven Chemical Discovery. *Chem. Sci.* **2019**, *10*, 7913-7922.
72. Liu, F.; Duan, C.; Kulik, H. J., Rapid Detection of Strong Correlation with Machine Learning for Transition-Metal Complex High-Throughput Screening. *J. Phys. Chem. Lett.* **2020**, *11*, 8067-8076.
73. Taylor, M. G.; Yang, T.; Lin, S.; Nandy, A.; Janet, J. P.; Duan, C.; Kulik, H. J., Seeing Is Believing: Experimental Spin States from Machine Learning Model Structure Predictions. *J. Phys. Chem. A* **2020**, *124*, 3286-3299.
74. Gugler, S.; Janet, J. P.; Kulik, H. J., Enumeration of De Novo Inorganic Complexes for Chemical Discovery and Machine Learning. *Mol. Sys. Des. Eng.* **2020**, *5*, 139-152.
75. Allahyari, Z.; Oganov, A. R., Nonempirical Definition of the Mendeleev Numbers: Organizing the Chemical Space. *J. Phys. Chem. C* **2020**, *124*, 23867-23878.
76. Sundermann, A.; Reiher, M.; Schoeller, W. W., Isoelectronic Arduengo-Type Carbene Analogues with the Group Iiiia Elements Boron, Aluminum, Gallium, and Indium. *Eur. J. Inorg. Chem.* **1998**, *1998*, 305-310.
77. Mastalir, M.; Glatz, M.; Gorgas, N.; Stöger, B.; Pittenauer, E.; Allmaier, G.; Veiros, L. F.; Kirchner, K., Divergent Coupling of Alcohols and Amines Catalyzed by Isoelectronic Hydride Mn^I and Fe^{II} PNP Pincer Complexes. *Chem. - Eur. J.* **2016**, *22*, 12316-12320.
78. Tang, H.; Brothers, E. N.; Hall, M. B., The Distinctive Electronic Structures of Rhenium Tris(Thiolate) Complexes, an Unexpected Contrast to the Valence Isoelectronic Ruthenium Tris(Thiolate) Complexes. *Inorg. Chem.* **2017**, *56*, 583-593.
79. Nandy, A.; Chu, D. B. K.; Harper, D. R.; Duan, C.; Arunachalam, N.; Cytter, Y.; Kulik, H. J., Large-Scale Comparison of 3d and 4d Transition Metal Complexes Illuminates the Reduced Effect of Exchange on Second-Row Spin-State Energetics. *Phys. Chem. Chem. Phys.* **2020**, *22*, 19326-19341.
80. Duan, C.; Liu, F.; Nandy, A.; Kulik, H. J., Data-Driven Approaches Can Overcome the Cost-Accuracy Tradeoff in Multireference Diagnostics. *J. Chem. Theory Comput.* **2020**, *16*, 4373-4387.
81. Duan, C.; Liu, F.; Nandy, A.; Kulik, H. J., Semi-Supervised Machine Learning Enables the Robust Detection of Multireference Character at Low Cost. *J. Phys. Chem. Lett.* **2020**, *11*, 6640-6648.
82. Li, X.; Chiong, R.; Page, A. J., Group and Period-Based Representations for Improved Machine Learning Prediction of Heterogeneous Alloy Catalysts. *J. Phys. Chem. Lett.* **2021**, *12*, 5156-5162.

83. Broto, P.; Moreau, G.; Vandycke, C., Molecular Structures: Perception, Autocorrelation Descriptor and Sar Studies: System of Atomic Contributions for the Calculation of the N-Octanol/Water Partition Coefficients. *Eur. J. Med. Chem.* **1984**, *19*, 71-78.
84. Janet, J. P.; Gani, T. Z. H.; Steeves, A. H.; Ioannidis, E. I.; Kulik, H. J., Leveraging Cheminformatics Strategies for Inorganic Discovery: Application to Redox Potential Design. *Ind. Eng. Chem. Res.* **2017**, *56*, 4898-4910.
85. Janet, J. P.; Kulik, H. J., Predicting Electronic Structure Properties of Transition Metal Complexes with Neural Networks. *Chem. Sci.* **2017**, *8*, 5137-5152.
86. Seritan, S.; Bannwarth, C.; Fales, B. S.; Hohenstein, E. G.; Kokkila-Schumacher, S. I.; Luehr, N.; Snyder Jr, J. W.; Song, C.; Titov, A. V.; Ufimtsev, I. S., Terachem: Accelerating Electronic Structure and Ab Initio Molecular Dynamics with Graphical Processing Units. *J. Chem. Phys.* **2020**, *152*, 224110.
87. Seritan, S.; Bannwarth, C.; Fales, B. S.; Hohenstein, E. G.; Isborn, C. M.; Kokkila-Schumacher, S. I.; Li, X.; Liu, F.; Luehr, N.; Snyder Jr, J. W., Terachem: A Graphical Processing Unit-Accelerated Electronic Structure Package for Large-Scale Ab Initio Molecular Dynamics. *Wiley Interdiscip. Rev.: Comput. Mol. Sci.* **2021**, *11*, e1494.
88. Becke, A. D., Density-Functional Thermochemistry. III. The Role of Exact Exchange. *J. Chem. Phys.* **1993**, *98*, 5648-5652.
89. Lee, C.; Yang, W.; Parr, R. G., Development of the Colle-Salvetti Correlation-Energy Formula into a Functional of the Electron Density. *Phys. Rev. B* **1988**, *37*, 785-789.
90. Stephens, P. J.; Devlin, F. J.; Chabalowski, C. F.; Frisch, M. J., Ab Initio Calculation of Vibrational Absorption and Circular Dichroism Spectra Using Density Functional Force Fields. *J. Phys. Chem.* **1994**, *98*, 11623-11627.
91. Hay, P. J.; Wadt, W. R., Ab Initio Effective Core Potentials for Molecular Calculations. Potentials for the Transition Metal Atoms Sc to Hg. *J. Chem. Phys.* **1985**, *82*, 270-283.
92. Ditchfield, R.; Hehre, W. J.; Pople, J. A., Self-Consistent Molecular-Orbital Methods. IX. An Extended Gaussian-Type Basis for Molecular-Orbital Studies of Organic Molecules. *J. Chem. Phys.* **1971**, *54*, 724.
93. Saunders, V. R.; Hillier, I. H., A "Level-Shifting" Method for Converging Closed Shell Hartree-Fock Wave Functions. *Int. J. Quantum Chem.* **1973**, *7*, 699-705.
94. Wang, L.-P.; Song, C., Geometry Optimization Made Simple with Translation and Rotation Coordinates. *J. Chem. Phys.* **2016**, *144*, 214108.
95. Ioannidis, E. I.; Gani, T. Z. H.; Kulik, H. J., molSimplify: A Toolkit for Automating Discovery in Inorganic Chemistry. *J. Comput. Chem.* **2016**, *37*, 2106-2117.
96. KulikGroup molSimplify & molSimplify Automatic Design. <https://github.com/hjkgrp/molsimplify> (accessed June 20, 2021).
97. O'Boyle, N. M.; Banck, M.; James, C. A.; Morley, C.; Vandermeersch, T.; Hutchison, G. R., Open Babel: An Open Chemical Toolbox. *J. Cheminf.* **2011**, *3*, 33.
98. O'Boyle, N. M.; Morley, C.; Hutchison, G. R., Pybel: A Python Wrapper for the Openbabel Cheminformatics Toolkit. *Chem. Cent. J.* **2008**, *2*, 5.
99. Pedregosa, F.; Varoquaux, G.; Gramfort, A.; Michel, V.; Thirion, B.; Grisel, O.; Blondel, M.; Prettenhofer, P.; Weiss, R.; Dubourg, V., Scikit-Learn: Machine Learning in Python. *J. Mach. Learn. Res.* **2011**, *12*, 2825-2830.
100. Tibshirani, R., Regression Shrinkage and Selection via the Lasso. *J. R. Stat. Soc. B* **1996**, *58*, 267-288.
101. Breiman, L., Random Forests. *Mach. Learn.* **2001**, *45*, 5-32.

For Table of Contents Use Only



**Supporting Information for
Representations and Strategies for Transferable Machine Learning Models in Chemical
Discovery**

Daniel R. Harper^{1,2,#}, Aditya Nandy^{1,2,#}, Naveen Arunachalam¹, Chenru Duan^{1,2}, Jon Paul Janet¹,
and Heather J. Kulik^{1,*}

¹Department of Chemical Engineering, Massachusetts Institute of Technology, Cambridge, MA
02139

²Department of Chemistry, Massachusetts Institute of Technology, Cambridge, MA 02139

[#]These authors contributed equally.

Content

Table S1 Spin multiplicities studied for each metal and oxidation state	Page S3
Table S2 Enumeration details of cis TMCs included in the data set	Page S3
Table S3 Data count for data in the IMP set	Page S4
Table S4 Data count for data in the ILP set	Page S4
Figure S1 PCA of Z_{eff} features	Page S4
Figure S2 Top 10 PCs of RAC-155 and Z_{eff} autocorrelations	Page S5
Figure S3 Average feature-space distance, subdivided by metal type	Page S6
Table S5 Metrics for filtering geometry optimizations	Page S7
Table S6 Number of calculations excluded by each filtering step	Page S7
Table S7 Number of spin-splitting data points after pairing	Page S8
Table S8 Number of ΔE_{LD} calculations excluded after filtering	Page S8
Figure S4 Analysis and cutoff for electronic structure check	Page S9
Figure S5 Analysis of validation errors with CV	Page S10
Table S9 Hyperparameters for $\Delta E_{\text{I-L}}$ on the IMP set	Page S11
Table S10 Linear models for all properties in the IMP set	Page S12
Figure S6 Distribution $\Delta E_{\text{H-L/H-I/I-L}}$ by metal/oxidation state	Page S13
Figure S7 $3d/4d$ parity plots for $\Delta E_{\text{I-L}}$ by metal/oxidation state	Page S14
Figure S8 $3d/4d$ parity plots for $\Delta E_{\text{H-L}}$ by metal/oxidation state	Page S15
Figure S9 $3d/4d$ parity plots for $\Delta E_{\text{H-I}}$ by metal/oxidation state	Page S15
Table S11 Linear models of $\Delta E_{\text{H-L/H-I/I-L}}$ in the IMP data set by metal/oxidation state	Page S16
Table S12 Frequency of $\Delta E_{\text{H-L/H-I/I-L}}$ for each metal/oxidation state in the full data set	Page S17
Table S13 Linear models of ΔE_{LD} in IMP by metal/oxidation state	Page S18
Figure S10 Distribution of ΔE_{LD} values by metal/oxidation state	Page S19
Table S14 Frequency of ΔE_{LD} for each metal/oxidation state in the full data set	Page S20
Figure S11 $3d/4d$ parity plot for ΔE_{LD} by metal, oxidation state, and spin multiplicity	Page S21
Figure S12 Linear correlation by metal in ILP data set, represented graphically	Page S22
Table S15 Linear correlation by metal in ILP data set, tabulated	Page S23
Figure S13 Correlation by isovalent ligand in ILP data set, represented graphically	Page S23
Table S16 Correlation by isovalent ligand in ILP data set, tabulated	Page S24
Table S17 ΔE_{LD} in the ILP set by metal/oxidation state	Page S24
Table S18 ΔE_{LD} in the ILP set by isovalent ligand type	Page S24
Table S19 Single-row vs transfer performance for $\Delta E_{\text{H-L}}$ and ΔE_{LD} in the IMP data set	Page S25
Figure S14 Results of grouping $4d$ metals by type before inter-row learning	Page S26
Table S20 Errors for adding types of $4d$ metals to an inter-row model	Page S26
Figure S15 MUEs for each property and learning objective	Page S27

Table S21 MUEs and standard deviations for each property and learning objective	Page S28
Figure S16 Features selected for each property and learning objective	Page S29
Table S22 Feature fraction by type for each property and learning objective	Page S30
Table S23 Feature fraction at various depths for each property and learning objective	Page S31
Table S24 Average distance in the down-selected feature space of trained models	Page S32

Table S1. Definition of spin state multiplicities ($2S+1$) studied for complexes grouped by the formal d electron count of the transition metal. Only LS and IS states are defined for the d^3 and d^7 complexes.

d^x	3d $M^{(ox)}$	4d $M^{(ox)}$	LS	IS	HS
d^3	Cr ^{III}	Mo ^{III}	doublet	quartet	--
d^4	Cr ^{II} , Mn ^{III}	Mo ^{II} , Tc ^{III}	singlet	triplet	quintet
d^5	Mn ^{II} , Fe ^{III}	Tc ^{II} , Ru ^{III}	doublet	quartet	sextet
d^6	Fe ^{II} , Co ^{III}	Ru ^{II} , Rh ^{III}	singlet	triplet	quintet
d^7	Co ^{II}	Rh ^{II}	doublet	quartet	--

Table S2. Ligand combinations enumerated for the cis arrangement (i.e., $M(L1)_4(L2)_2$) in the final data set. Each ligand combination is used with 12 metal and oxidation state combinations: Cr^{II}/Mo^{II}, Mn^{II/III}/Tc^{II/III}, Fe^{II/III}/Ru^{II/III}, and Co^{III}/Rh^{III} in 3 possible spin states (i.e., no Cr^{III}/Mo^{III} and Co^{II}/Rh^{II} which are only in two spin states) for a total of 36 TMCs per ligand combination. This leads to 1080 TMCs with ligands in the cis arrangement considered.

#	L1 (eq. and ax.)	L2 (eq.)
1	acetonitrile	methyl isocyanide
2	ammonia	acetonitrile
3	ammonia	carbonyl
4	ammonia	chloride
5	ammonia	cyanide
6	ammonia	fluoride
7	ammonia	hydrogen sulfide
8	ammonia	methyl isocyanide
9	ammonia	phosphine
10	ammonia	water
11	carbonyl	cyanide
12	chloride	hydrogen sulfide
13	chloride	phosphine
14	cyanide	carbonyl
15	fluoride	ammonia
16	fluoride	water
17	hydrogen sulfide	chloride
18	hydrogen sulfide	phosphine
19	methyl isocyanide	acetonitrile
20	phosphine	chloride
21	phosphine	hydrogen sulfide
22	water	acetonitrile
23	water	ammonia
24	water	carbonyl
25	water	chloride
26	water	cyanide
27	water	fluoride
28	water	hydrogen sulfide
29	water	methyl isocyanide
30	water	phosphine

Table S3. Isovalent metal pairing (IMP) data set sizes for each property studied. From left to right: starting from the filtered total (i.e., retained TMCs), if a $3d$ or $4d$ TMC point is missing from a pair or if a pair fails the electronic structure (ES) check (i.e., from deviations in the d orbital populations), the points are eliminated. The final number of points and pairs (shown in parentheses) in each set is indicated.

Property	Filtered total ($3d$ and $4d$ TMCs)	$3d$ or $4d$ missing from pair	eliminated by ES check	Final # (# pairs)
ΔE_{H-L}	1,030	374	8	648 (324)
ΔE_{I-L}	1,853	507	86	1,260 (630)
ΔE_{H-I}	961	389	18	554 (277)
ΔE_{LD}	2,788	430	244	2114 (1057)

Table S4. Isovalent ligand pairing (ILP) data set sizes for each property studied. Starting from the filtered (i.e., retained TMCs), if a $3d$ or $4d$ TMC point is missing from a pair or if a pair fails the electronic structure (ES) check, (i.e., from deviations in the d orbital populations), the points are eliminated. The final number of points and pairs (shown in parentheses) in each set is indicated.

Property	Filtered total ($3d$ and $4d$ TMCs)	missing from isovalent ligand pair	eliminated by E.S. check	Final # (# pairs)
ΔE_{H-L}	1,030	630	40	360 (180)
ΔE_{I-L}	1,853	1,053	158	642 (321)
ΔE_{H-I}	961	609	16	336 (168)
ΔE_{LD}	2,788	1,452	244	1,092 (546)

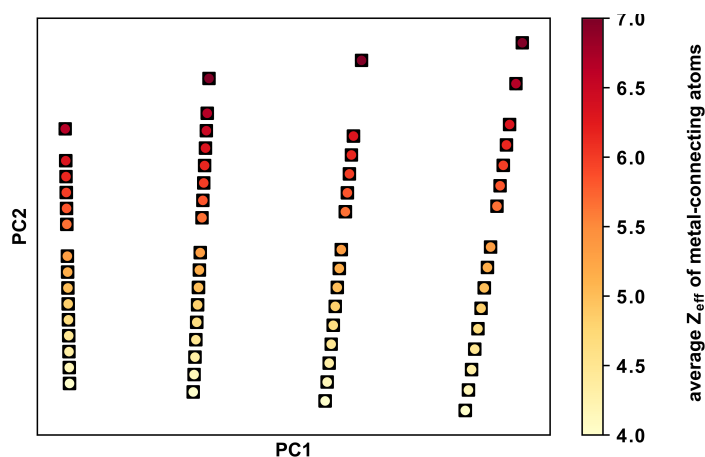


Figure S1. Principal component analysis of metal-centered features constructed from a subset of Z_{eff} mc-RACs (i.e., $d = 0$ or 1). The 1853 data points (i.e., from IMP ΔE_{I-L}) are colored based on the average Z_{eff} of metal-connecting ligand atoms (many points overlap). The first PC differentiates TMCs based on the group number of the metal atom, and the second PC by the group number of the metal-connecting ligand atom.

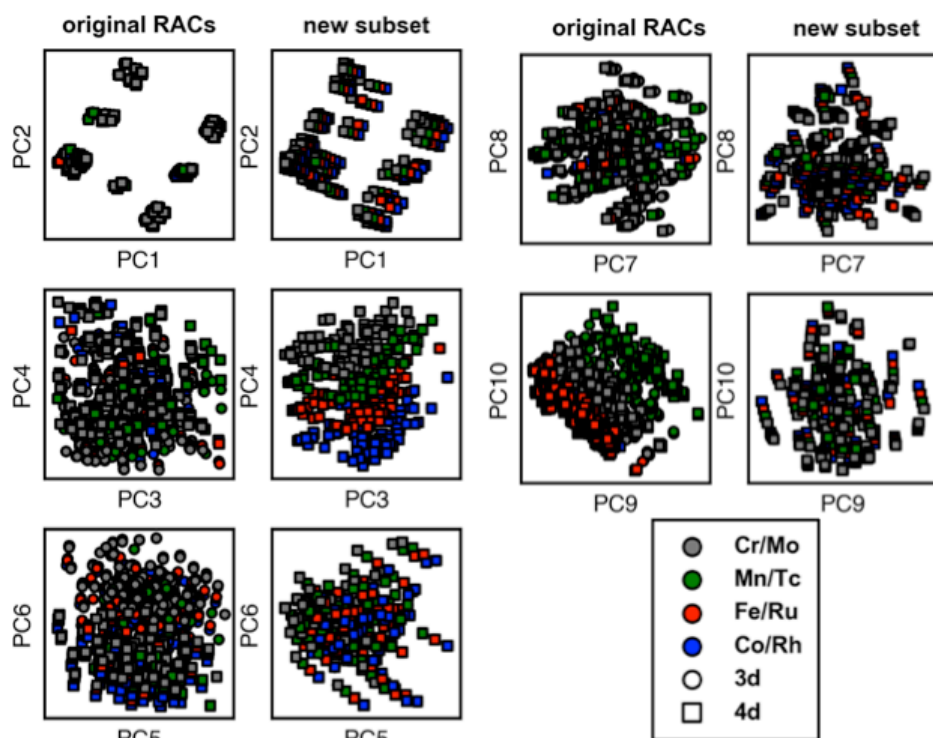


Figure S2. PCA of the ΔE_{I-L} points in the IMP data set for the RAC-155 representation (original RACs, columns 1 and 3) and the 33 RACs based on the Z_{eff} atomic property (new subset, columns 2 and 4). All points are colored according to inset legend. The symbol indicates the metal center's row on the periodic table, and $3d$ and $4d$ points overlap in the new subset representation. The fourth PC highlights the key distinction between original RACs and the new features.

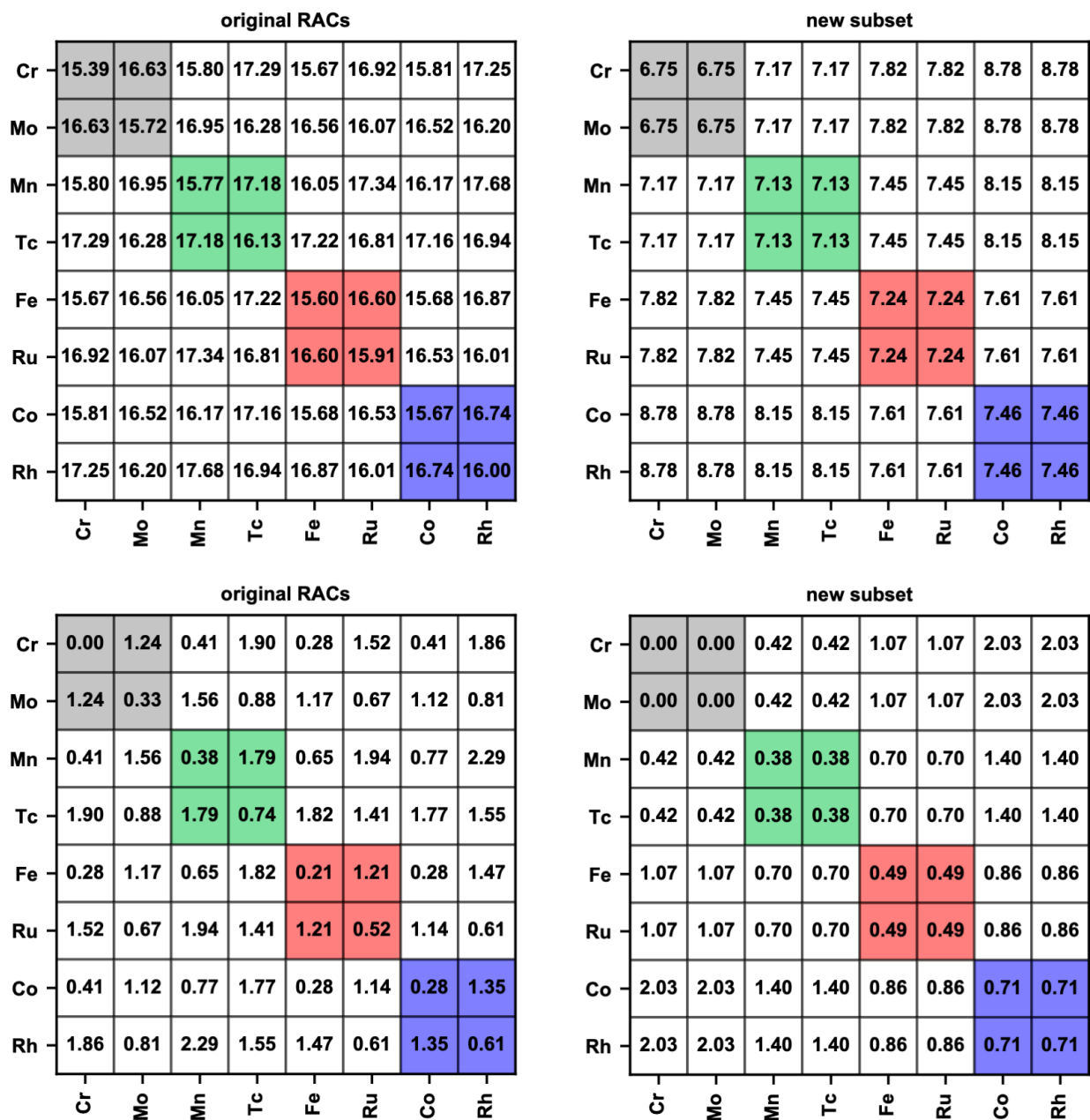


Figure S3. Average Euclidean distance (top) among complexes in the ΔE_{I-L} portion of the IMP data set grouped by metal along with the average Euclidean distance after subtracting the minimum value in the matrices (bottom). These properties are shown for the RAC-155 representation (left) along with the 33 added RACs with Z_{eff} (right).

Table S5. Geometry check parameters employed to determine if calculations converged to a suitable octahedral geometry. Cutoffs for final calculations, along with loose cutoffs employed during resubmission (indicated in parentheses) are listed: coordination number of 6 (i.e., as judged through interatomic distances being within 1.37 Å x the sum of the respective elements' covalent radii); first coordination sphere metrics including the mean and maximum (max.) deviation in the angle ($\Delta\theta(C_i-M-C_j)$) formed with coordinating atoms (C_i or C_j) and the metal from the expected values of 90° or 180° as well as the maximum overall difference between metal-coordinating atom bond lengths over all ligands in the equatorial (eq.) plane; ligand distortion metrics including the maximum root mean square deviation (RMSD) of any atom from the starting structure. For ligands that are expected to be linear, additional checks are applied on the deviation of the angle formed by the metal and the first two atoms of the ligand (A, B) from 180°. Tightened checks for homoleptic TMCs are indicated for $\max(\Delta d)$ with a special threshold for singlet states due to our expectation of higher symmetry for these structures.

Coordination number			
6 (6)			
First coordination sphere			
$\text{mean}(\Delta\theta(C_i-M-C_j))$ 12° (16°)	$\text{max}(\Delta\theta(C_i-M-C_j))$ 22.5° (27.0°)	$\text{max}(\Delta d)$ 1.00 Å (1.25 Å) homoleptic: 0.4 Å (1.25 Å) homoleptic singlets: 0.2 Å (1.25 Å)	$\text{max}(\Delta d_{\text{eq}})$ 0.35 Å (0.45 Å)
Ligand distortion metrics			
$\text{max}(\text{RMSD})$ 0.30 Å (0.40 Å)		$\text{mean}(\Delta\theta(M-A-B))$ 20° (30°)	$\text{max}(\Delta\theta(M-A-B))$ 28° (40°)

Table S6. Number of data points for 3d or 4d TMCs eliminated at each sequential filtering step. For both 3d and 4d TMCs, the initial pool of candidates, number of points retained after each filtering step, and the number of points eliminated at that step are all listed. Cumulative totals of eliminated complexes are listed as “overall.” The filtering steps were: i) checking for convergence (completion, passing loose thresholds upon five 24-hour job resubmissions), ii) checking geometries against defined metrics, with different criteria for heteroleptic and homoleptic complexes, iii) checking for deviations of $\langle S^2 \rangle$ from the expected value by more than $1 \mu_B^2$, and iv) checking for deviations of metal spin from the total spin of more than $1 \mu_B$.

Check Performed	3d TMCs		4d TMCs	
	Retained	Eliminated at step	Retained	Eliminated at step
Start	4,720	--	4,720	--
Converged	4,282	418	4,447	273
Geometry (Heteroleptic)	3,487	795	3,028	1,419
Geometry (Homoleptic)	3,479	8	3,001	27
$\langle S^2 \rangle$	3,335	144	2,939	62
Metal spin	3,197	138	2,795	144
Overall	3,197	1,523	2,795	1,925

Table S7. From the converged geometry optimizations that pass all checks, the number of pairs of ΔE_{H-L} , ΔE_{I-L} , and ΔE_{H-I} adiabatic spin-splitting energies that can be evaluated for 3d and 4d TMCs (i.e., both spin states converged and passed filtering checks). For the earliest Cr(III)/Mo(III) and latest Co(II)/Rh(II) metal/oxidation state pairs, only ΔE_{I-L} is defined.

Category	ΔE_{H-L}	ΔE_{I-L}	ΔE_{H-I}
All converged points	3163	4408	2652
-Missing one point	1103	702	730
Final ΔE pairs	1030	1853	961

Table S8. Number of ΔE_{LD} 3d or 4d TMC data points eliminated after filtering on deviations of $\langle S^2 \rangle$ or the metal center spin of the TMC with the ligand dissociated (dissoc. TMC). We evaluate this property for the subset of TMCs with trans and homoleptic symmetry to avoid uncertainty about which axial ligand to dissociate and only study cases with neutral ligands to avoid changing charge of the TMC upon ligand removal.

Filtering step	3d TMCs		4d TMCs	
	Retained	Eliminated at step	Retained	Eliminated at step
Retained octahedral TMCs	3,197	--	2,795	--
Dissoc. TMC $\langle S^2 \rangle$	3,156	41	2,767	28
Dissoc. TMC M spin	3,140	16	2,398	369
Trans and homoleptic TMCs only	1,934	1,206	1,659	739
Neutral ligands only	1,500	434	1,288	371
Overall	1,500	1,697	1,288	1,507

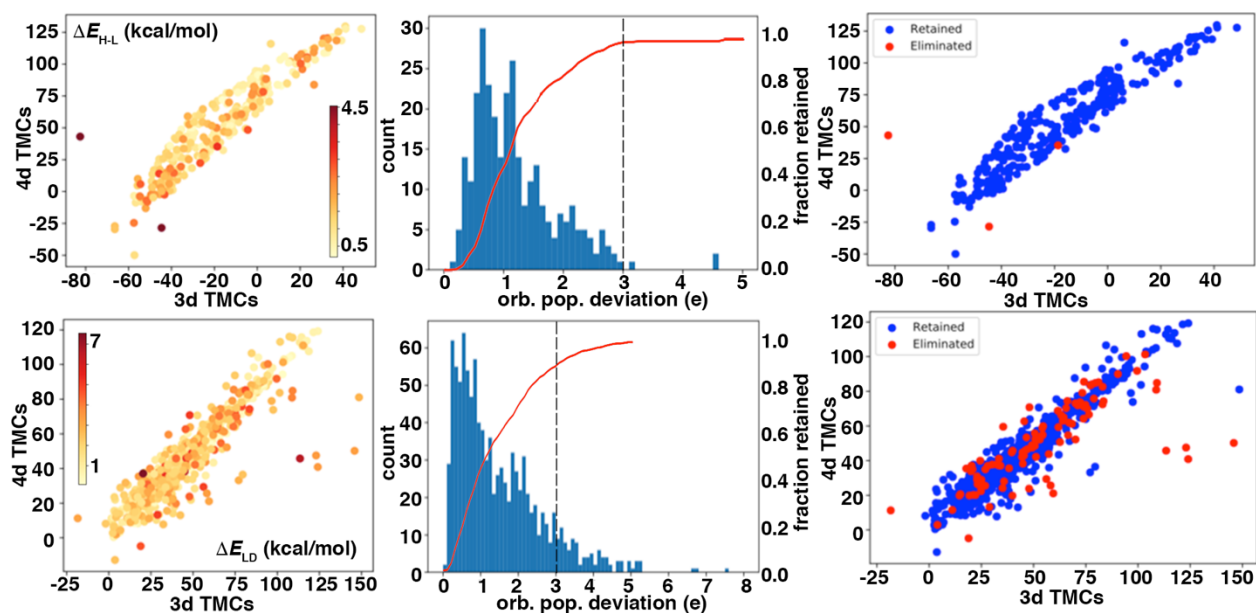


Figure S4. The heuristic cutoff for the orbital population (orb. pop.) deviation check was chosen based on the relationships between differences and properties for ΔE_{H-L} and ΔE_{LD} in the IMP data set. The difference in d -orbital occupations from NBO analysis is shown (left) and colored according to the inset color bars. The chosen value (3 e^-) eliminates cases where the deviation in orbital populations is most extreme (middle pane, fraction retained shown as red line with right axis). The right pane shows the data distinguishing the points that are eliminated (red) or retained (blue) using our heuristic cutoff 3 e^- , with both properties shown in kcal/mol.

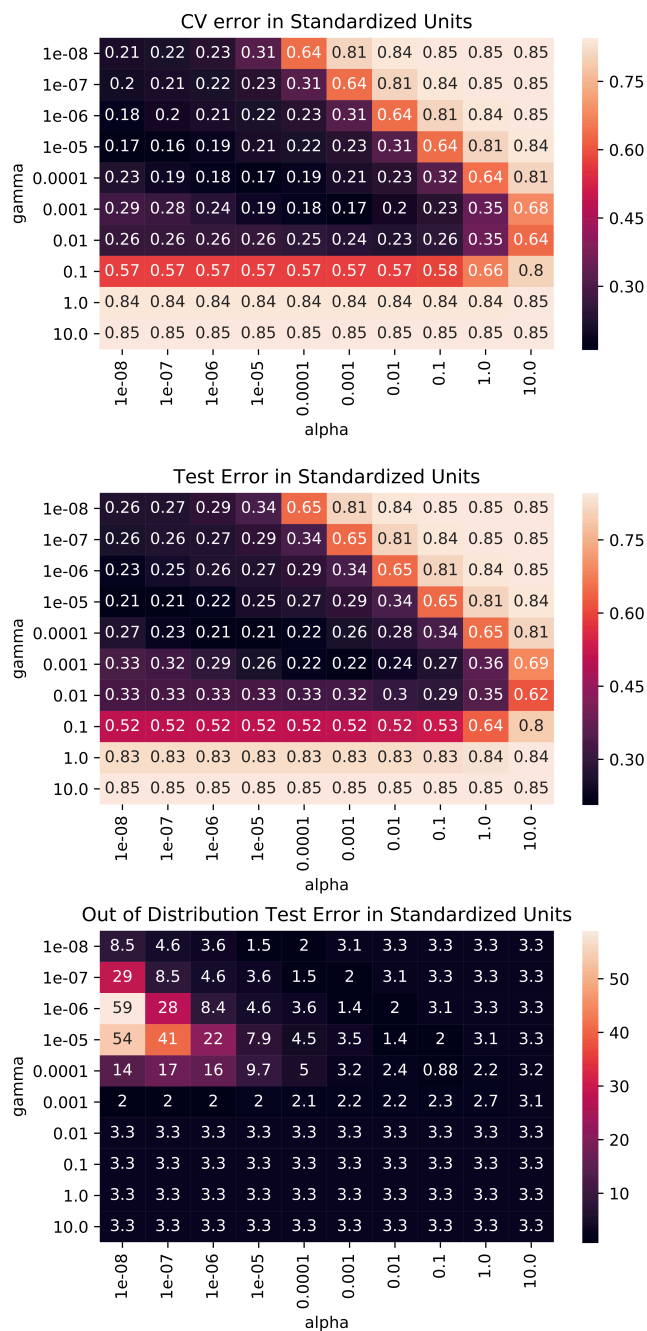


Figure S5. Evaluation of KRR model errors for the 324-complex-pair IMP dataset for ΔE_{H-L} with eRAC-185. The model was trained only on 80% $3d$ data, and an in-distribution test set is the remaining 20% of the $3d$ data. An out-of-distribution test set is the 20% $4d$ data that correspond to the isovalent pairs to the in-distribution 20% $3d$ test data. The comparison of error evaluations includes 10-fold cross validation (top) on the $3d$ complexes in training, error on the in-distribution test set (middle), and an out of distribution test set (bottom). In all cases, the comparisons are for α and γ hyperparameters from a grid search. Since CV errors do not reflect the out-of-distribution test set errors, we select hyperparameters directly based on the validation set in this work.

Table S9. Hyperparameters (α and γ) selected for an ensemble of 25 KRR models predicting the ΔE_{I-L} property (524 $3d$ TMC points in train) in the IMP set when 20 $4d$ TMC points are included in the training set. All models use the eRAC-185 representation as a starting point and retain the features in this case from a 1% cutoff of a random forest model (RF_cutoff). The test MUE (on the 20% set aside $4d$ TMC points) of each model is reported along with ensemble average and standard deviation over all 25 models. Hyperparameters for models predicting other properties, using different data sets, and including a different number of training points from the same row as the validation data are provided in the Supporting Information .zip as .csv files.

Model Number	Feature Selection	α	γ	Test MUE (kcal/mol)
1	RF_cutoff	1.00E-11	1.00E-07	7.59
2	RF_cutoff	1.00E-11	1.00E-06	7.09
3	RF_cutoff	1.00E-05	1.00E-04	7.14
4	RF_cutoff	1.00E-04	1.00E-03	7.07
5	RF_cutoff	1.00E-08	1.00E-04	8.27
6	RF_cutoff	1.00E-07	1.00E-04	7.27
7	RF_cutoff	1.00E-03	1.00E-02	8.76
8	RF_cutoff	1.00E-11	1.00E-07	9.72
9	RF_cutoff	1.00E-05	1.00E-03	9.24
10	RF_cutoff	1.00E-03	1.00E-03	9.07
11	RF_cutoff	1.00E-04	1.00E-03	8.09
12	RF_cutoff	1.00E-02	1.00E-02	6.93
13	RF_cutoff	1.00E-07	1.00E-04	8.82
14	RF_cutoff	1.00E-11	1.00E-06	8.09
15	RF_cutoff	1.00E-05	1.00E-04	7.71
16	RF_cutoff	1.00E-09	1.00E-05	7.52
17	RF_cutoff	1.00E-03	1.00E-03	10.91
18	RF_cutoff	1.00E-08	1.00E-04	9.41
19	RF_cutoff	1.00E-05	1.00E-04	8.53
20	RF_cutoff	1.00E-03	1.00E-02	8.22
21	RF_cutoff	1.00E-05	1.00E-03	7.43
22	RF_cutoff	1.00E-11	1.00E-07	8.55
23	RF_cutoff	1.00E-11	1.00E-06	10.97
24	RF_cutoff	1.00E-12	1.00E-07	7.95
25	RF_cutoff	1.00E-06	1.00E-04	9.06
Ensemble				8.38±1.11

Table S10. Linear models ($y = ax+b$, a , unitless, and b , in kcal/mol) for properties of $3d$ TMCs (x) to $4d$ TMCs (y) in the IMP data set (set sizes shown as # points). The mean unsigned error (MUE) in predicting the $4d$ metal property from the $3d$ metal property using the linear model is reported along with the number of points in the set. Lines were fit using ordinary least squares, and the R^2 value for each line is shown.

Property	a	b	R^2	MUE (kcal/mol)	# points
ΔE_{H-L}	1.41	75.65	0.89	9.69	324
ΔE_{I-L}	1.38	27.45	0.91	7.06	630
ΔE_{H-I}	0.97	40.96	0.65	6.14	277
ΔE_{LD}	0.93	3.75	0.91	4.88	1057

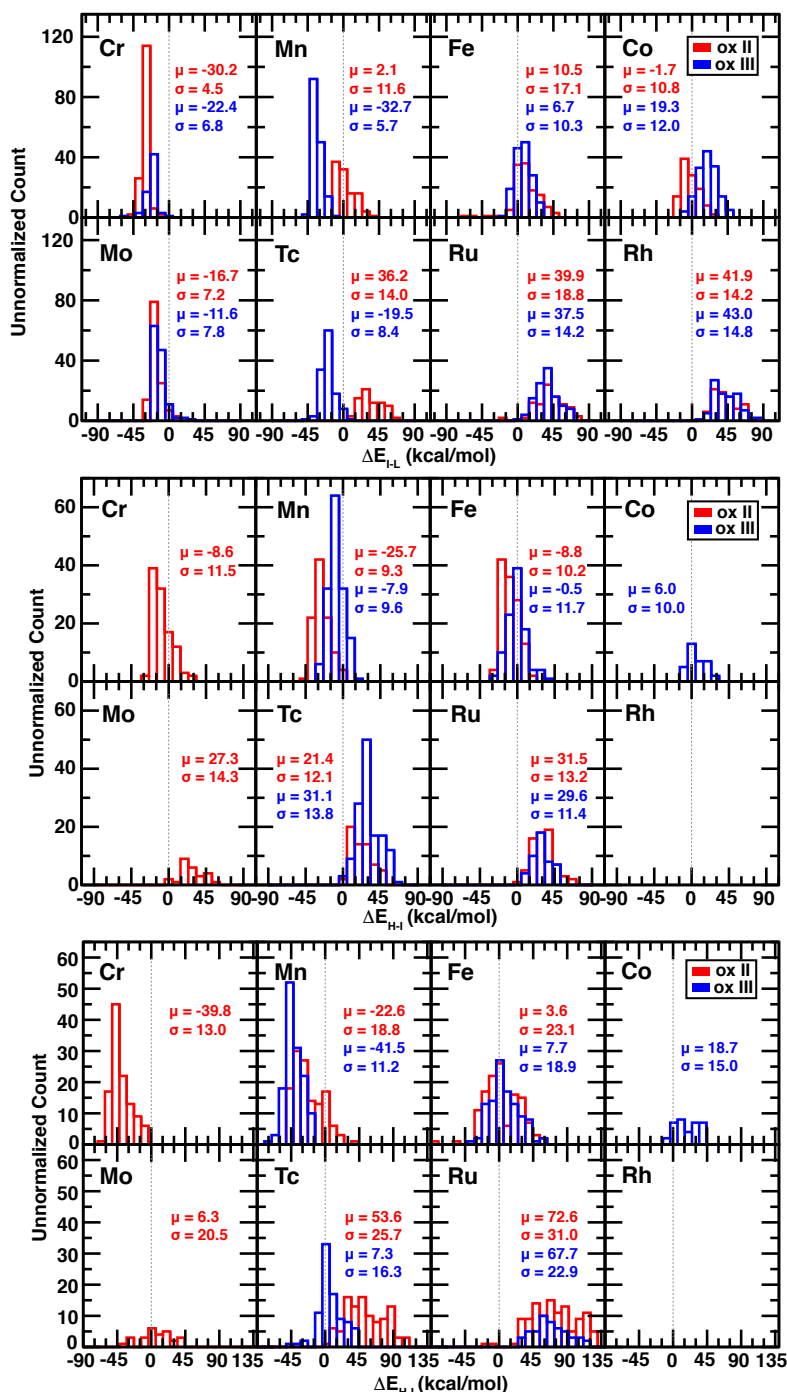


Figure S6. Distribution of adiabatic ΔE spin-splitting (in kcal/mol) for 3d TMCs (upper panes) and 4d TMCs (lower panes) in the full data set prior to the ILP or IMP pairing. Data is grouped by spin states and differences in number of paired electrons between states: 2-electron LS-IS (top), 2-electron IS-HS (middle), and 4-electron LS-HS (bottom). The zero value is shown as a vertical dashed line within each pane. Distributions are colored by oxidation state: II (red) and III (blue). Mean values (μ , in kcal/mol) and standard deviations (σ , in kcal/mol) of distributions are labeled within each pane by oxidation state. The majority of 4d TMCs favor LS states (positive values), whereas 3d TMC distributions have a higher population of higher-spin states (negative values).

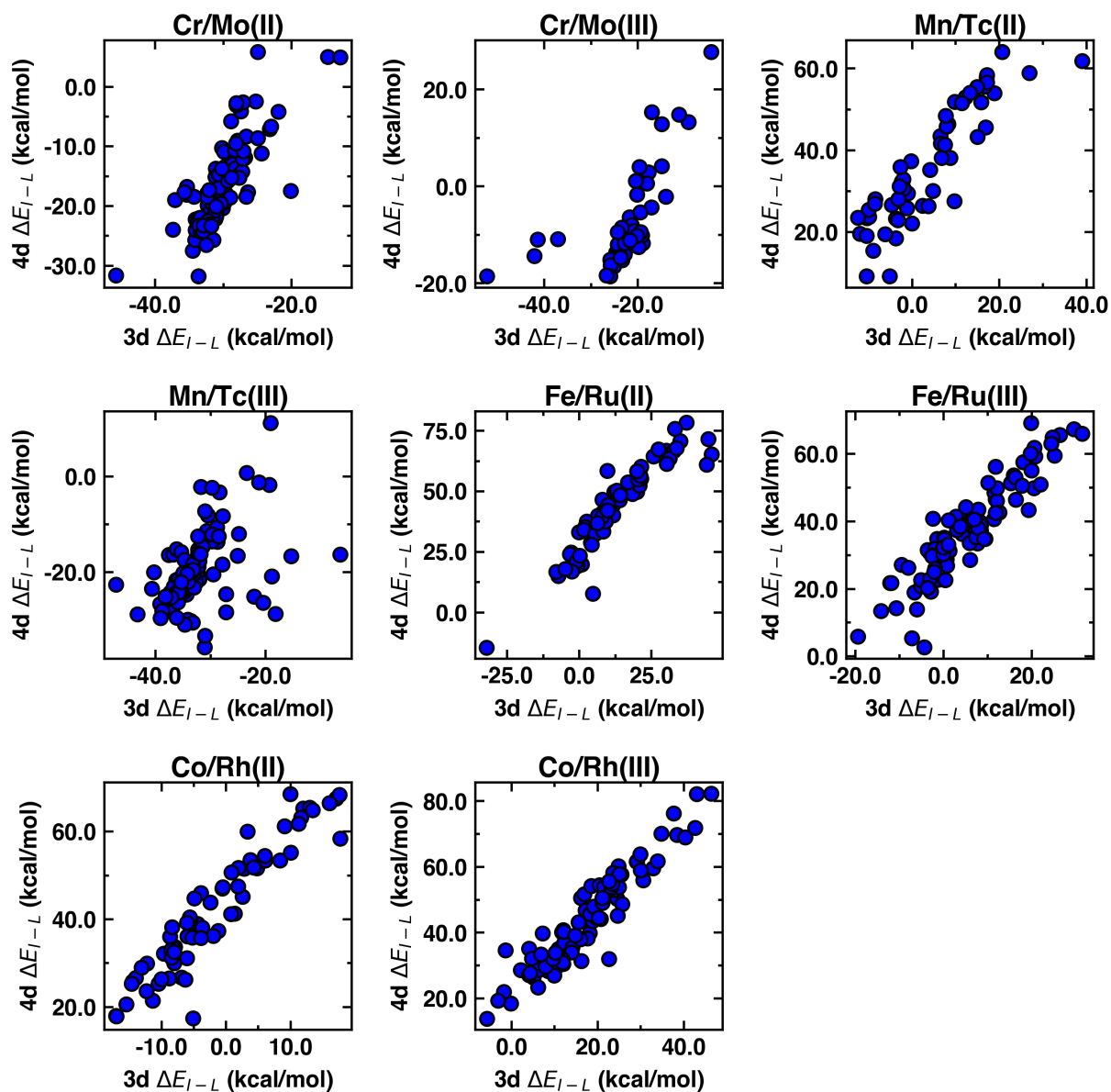


Figure S7. Parity plots of the 3d and 4d IS-LS spin-splitting, i.e., $3d \Delta E_{I-L}$ and $4d \Delta E_{I-L}$, (in kcal/mol) in the IMP data set. The range of the graphs is set to be the largest range in the data, which varies by metal and oxidation state and can be larger for one of the two axes.

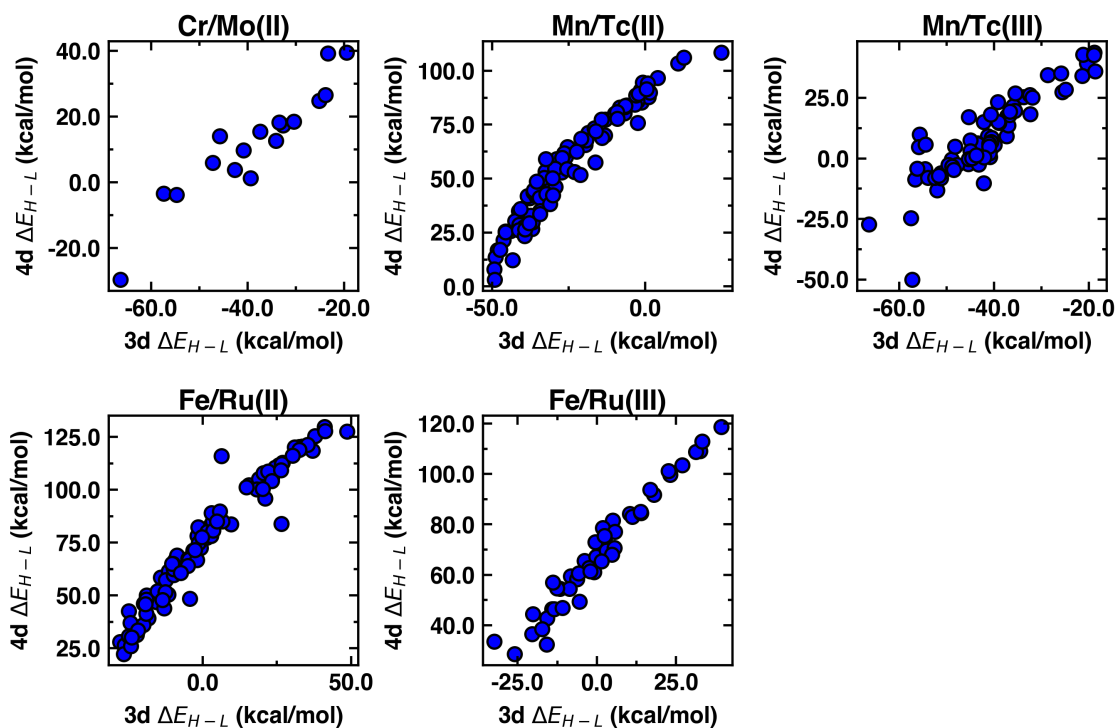


Figure S8. Parity plots of the 3d and 4d HS-LS spin-splitting, i.e., $3d \Delta E_{H-L}$ and $4d \Delta E_{H-L}$, (in kcal/mol) in the IMP data set. The range of the graphs is set to be the largest range in the data, which varies by metal and oxidation state and can be larger for one of the two axes.

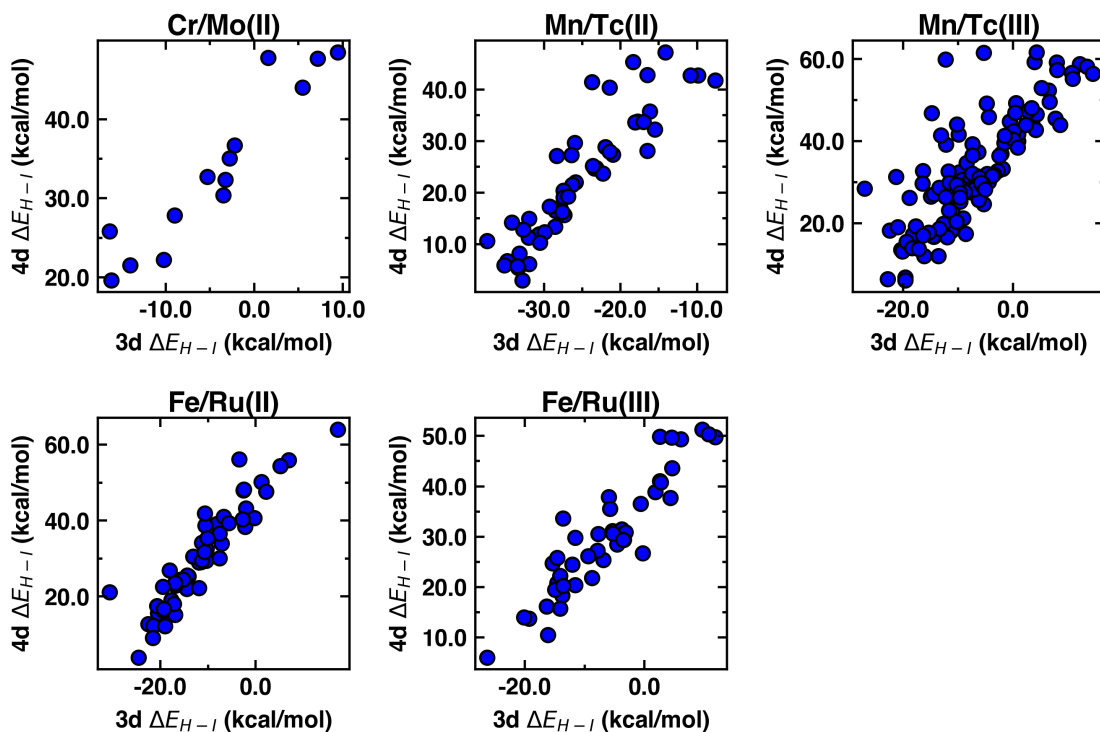


Figure S9. Parity plots of the 3d and 4d HS-IS spin-splitting, i.e., $3d \Delta E_{H-I}$ and $4d \Delta E_{H-I}$, (in kcal/mol) in the IMP data set. The range of the graphs is set to be the largest range in the data, which varies by metal and oxidation state and can be larger for one of the two axes.

Table S11. Linear models ($y = ax + b$, a , unitless, and b , in kcal/mol) relating $3d$ (x) and $4d$ (y) spin-splitting properties (specific spin states are annotated in table) for complexes in the IMP set by metal (M) and oxidation (ox) state. Models are only reported if at least five data points are available. The mean unsigned error (MUE) in predicting the $4d$ metal property from the $3d$ metal property using the linear model is reported along with the number of points in the set. Lines were fit using ordinary least squares, and the R^2 value for each line is shown.

ΔE_{H-L}						
M(ox)		Linear Model		R^2	MUE (kcal/mol)	# points
x	y	a	b			
Cr(II)	Mo(II)	1.21	58.78	0.88	4.68	17
Mn(III)	Tc(III)	1.45	68.70	0.79	5.41	71
Mn(II)	Tc(II)	1.47	91.35	0.94	5.06	96
Fe(III)	Ru(III)	1.36	67.35	0.96	3.62	47
Fe(II)	Ru(II)	1.45	73.47	0.93	5.27	93
Average MUE		--	--	--	4.81	--
ΔE_{I-L}						
M(ox)		Linear Model		R^2	MUE (kcal/mol)	# points
x	y	a	b			
Cr(III)	Mo(III)	0.88	11.71	0.44	5.59	60
Cr(II)	Mo(II)	1.35	24.21	0.61	3.30	104
Mn(III)	Tc(III)	0.59	-0.89	0.2	5.30	96
Mn(II)	Tc(II)	1.16	31.78	0.79	5.43	55
Fe(III)	Ru(III)	1.27	30.38	0.84	4.48	94
Fe(II)	Ru(II)	1.19	28.35	0.86	4.83	68
Co(III)	Rh(III)	1.27	21.81	0.88	4.05	86
Co(II)	Rh(II)	1.47	44.45	0.89	3.60	67
Average MUE		--	--	--	4.57	--
ΔE_{H-I}						
M(ox)		Linear Model		R^2	MUE (kcal/mol)	# points
x	y	a	b			
Cr(II)	Mo(II)	1.14	38.57	0.89	2.17	14
Mn(III)	Tc(III)	1.22	41.74	0.64	6.05	114
Mn(II)	Tc(II)	1.55	61.77	0.82	3.80	51
Fe(III)	Ru(III)	1.20	37.68	0.85	3.20	44
Fe(II)	Ru(II)	1.40	46.37	0.85	3.69	54
Average MUE		--	--	--	3.78	--

Table S12. Frequency of metal and oxidation state combinations in the filtered data sets for 3*d* and 4*d* TMC adiabatic ΔE pairs grouped by 4-electron ΔE_{H-L} , 2-electron ΔE_{I-L} , and 2-electron ΔE_{H-I} . When a spin state in the definition is undefined, no data was collected and -- is indicated, whereas when no data was converged and retained, a zero is indicated. Fewer late TMCs have converged ΔE values that involve high-spin states.

Full Set							
3 <i>d</i>	4 e H-L	2 e I-L	2 e H-I	4 <i>d</i>	4 e H-L	2 e I-L	2 e H-I
Cr(III)	--	67	--	Mo(III)	--	126	--
Cr(II)	110	149	106	Mo(II)	27	128	26
Mn(III)	136	158	148	Tc(III)	188	125	137
Mn(II)	129	105	101	Tc(II)	103	75	62
Fe(III)	107	153	101	Ru(III)	50	113	47
Fe(II)	127	123	125	Ru(II)	113	91	70
Co(III)	34	146	33	Rh(III)	0	96	0
Co(II)	--	110	--	Rh(II)	--	71	--
IMP Set							
Cr(III)	--	60	--	Mo(III)	--	60	--
Cr(II)	17	104	14	Mo(II)	17	104	14
Mn(III)	71	96	114	Tc(III)	71	96	114
Mn(II)	96	55	51	Tc(II)	96	55	51
Fe(III)	47	94	44	Ru(III)	47	94	44
Fe(II)	93	68	54	Ru(II)	93	68	54
Co(III)	0	86	0	Rh(III)	0	86	0
Co(II)	--	67	--	Rh(II)	--	67	--
ILP Set							
Cr(III)	--	11	--	Mo(III)	--	30	--
Cr(II)	21	26	26	Mo(II)	1	14	2
Mn(III)	27	34	36	Tc(III)	12	15	32
Mn(II)	31	14	16	Tc(II)	27	9	10
Fe(III)	8	28	7	Ru(III)	2	15	2
Fe(II)	26	21	25	Ru(II)	25	15	12
Co(III)	0	34	0	Rh(III)	0	12	0
Co(II)	--	28	--	Rh(II)	--	15	--

Table S13. Linear models ($y = ax + b$, a , unitless, and b , in kcal/mol) relating $3d$ (x) and $4d$ (y) ΔE_{LD} properties for complexes in the IMP set by metal (M), oxidation (ox) state, and spin multiplicity ($2S+1$). Models are only reported if at least five data points are available. The mean unsigned error (MUE) in predicting the $4d$ metal property from the $3d$ metal property using the linear model is reported along with the number of points in the set. Lines were fit using ordinary least squares, and the R^2 value for each line is shown.

M(ox)	2S+1	Linear Model		R ²	MUE (kcal/mol)	# points
		a	b			
Cr(III)	2	0.90	3.31	0.88	8.95	23
Cr(III)	4	0.92	5.30	1.00	1.07	67
Cr(II)	1	0.88	9.91	0.85	3.10	44
Cr(II)	3	0.83	10.53	0.93	2.36	75
Cr(II)	5	0.89	0.22	0.41	7.79	13
Mn(III)	1	0.90	7.28	0.93	5.15	37
Mn(III)	3	0.95	5.22	0.98	2.44	74
Mn(III)	5	1.01	-4.14	0.94	4.96	59
Mn(II)	2	0.90	10.37	0.92	2.44	69
Mn(II)	4	0.75	6.20	0.62	7.87	29
Mn(II)	6	0.92	-1.71	0.97	1.33	55
Fe(III)	2	0.92	6.95	0.98	2.27	81
Fe(III)	4	0.96	-1.10	0.93	4.84	34
Fe(III)	6	0.94	-3.22	0.99	0.98	23
Fe(II)	1	0.80	11.38	0.84	2.39	68
Fe(II)	3	0.90	1.39	0.85	5.80	40
Fe(II)	5	0.88	0.27	0.97	1.56	51
Co(III)	1	0.80	12.50	0.88	3.39	92
Co(III)	3	0.95	1.96	0.90	5.88	38
Co(II)	2	0.88	3.68	0.74	6.42	38
Co(II)	4	0.79	3.23	0.94	1.69	47
Average	--	--	--	--	3.94	--

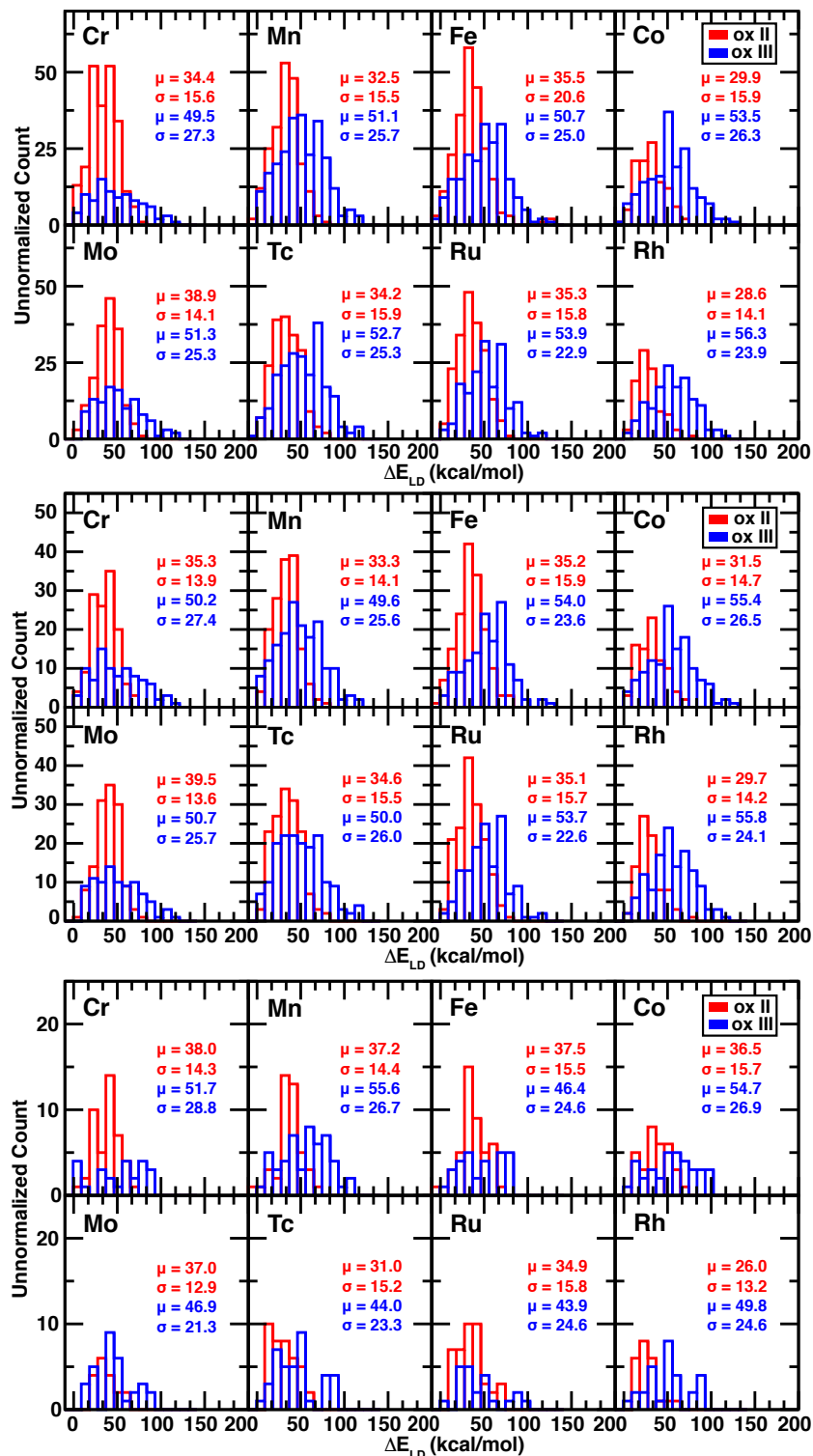


Figure S10. Distribution of ΔE_{LD} (in kcal/mol) for 3d TMCs (upper panes) and 4d TMCs (lower panes) in the full data set (top), IMP (middle), and ILP (bottom) data sets. Distributions are colored by oxidation state: II (red) and III (blue). Mean values (μ , in kcal/mol) and standard deviations (σ , in kcal/mol) of distributions are labeled within each pane by oxidation state.

Table S14. Frequency of metal, oxidation, and spin-state combinations for the ΔE_{LD} property in the full data set, the IMP data set, and the ILP data set, as indicated in the table below. When a spin state in the definition is undefined, no data was collected and -- is indicated, whereas when no data was converged and retained, a zero is indicated.

Full Set							
3d	LD			4d	LD		
	LS	IS	HS		LS	IS	HS
Cr(III)	27	67	--	Mo(III)	42	68	--
Cr(II)	83	77	67	Mo(II)	73	82	15
Mn(III)	83	86	76	Tc(III)	59	92	67
Mn(II)	74	59	74	Tc(II)	86	47	55
Fe(III)	85	76	50	Ru(III)	93	54	23
Fe(II)	81	74	73	Ru(II)	89	47	62
Co(III)	94	73	11	Rh(III)	93	46	0
Co(II)	52	58	--	Rh(II)	44	51	--
IMP Set							
Cr(III)	23	67	--	Mo(III)	23	67	--
Cr(II)	44	75	13	Mo(II)	44	75	13
Mn(III)	37	74	59	Tc(III)	37	74	59
Mn(II)	69	29	55	Tc(II)	69	29	55
Fe(III)	81	34	23	Ru(III)	81	34	23
Fe(II)	68	40	51	Ru(II)	68	40	51
Co(III)	92	38	0	Rh(III)	92	38	0
Co(II)	38	47	--	Rh(II)	38	47	--
ILP Set							
Cr(III)	6	42	--	Mo(III)	18	44	--
Cr(II)	24	30	34	Mo(II)	14	20	2
Mn(III)	30	40	32	Tc(III)	16	32	30
Mn(II)	30	14	42	Tc(II)	32	14	32
Fe(III)	32	22	4	Ru(III)	38	6	0
Fe(II)	22	36	32	Ru(II)	38	22	24
Co(III)	33	26	0	Rh(III)	50	8	0
Co(II)	28	36	--	Rh(II)	24	22	--

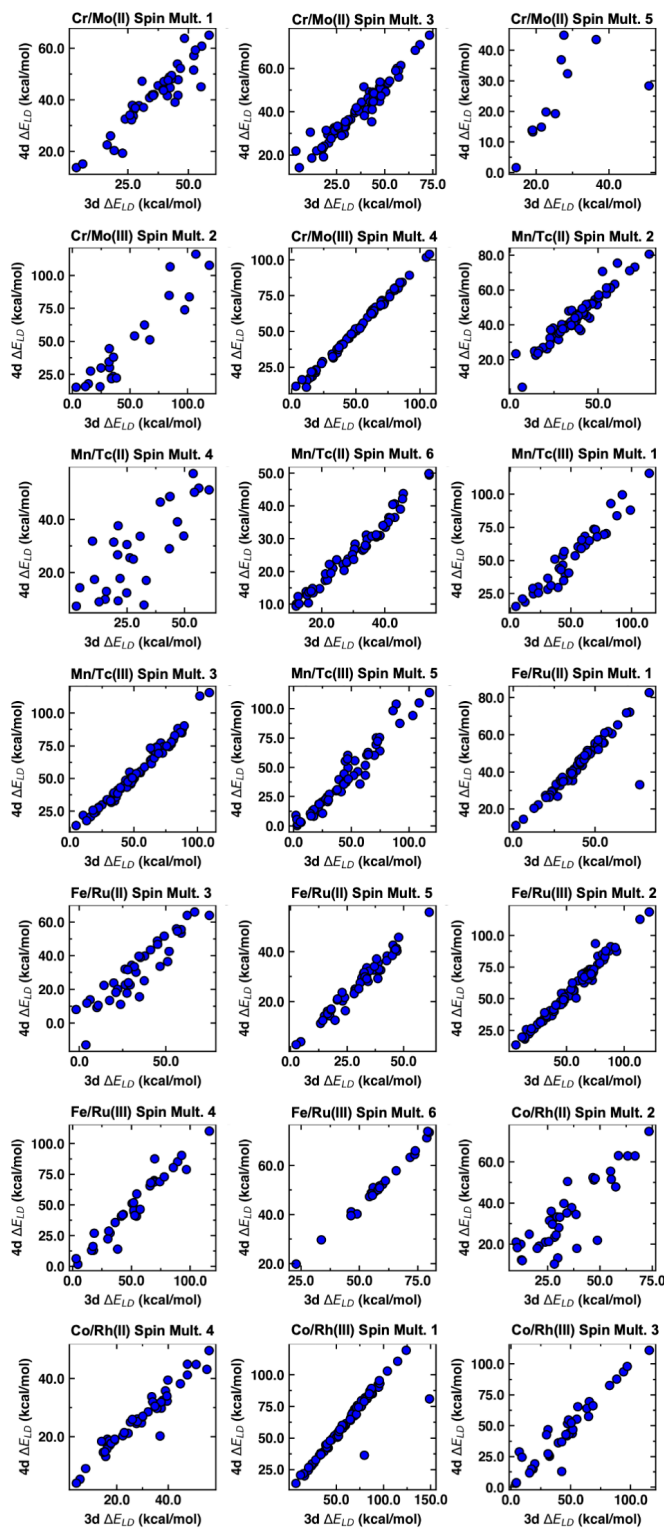


Figure S11. Parity plots of the $3d$ to $4d$ ΔE_{LD} (in kcal/mol) in the IMP data set. Sets are distinguished by metal/oxidation state and spin multiplicity (Spin. Mult.). The range of the graphs is set to be the largest range in the data, which varies and can be larger for one of the two axes.

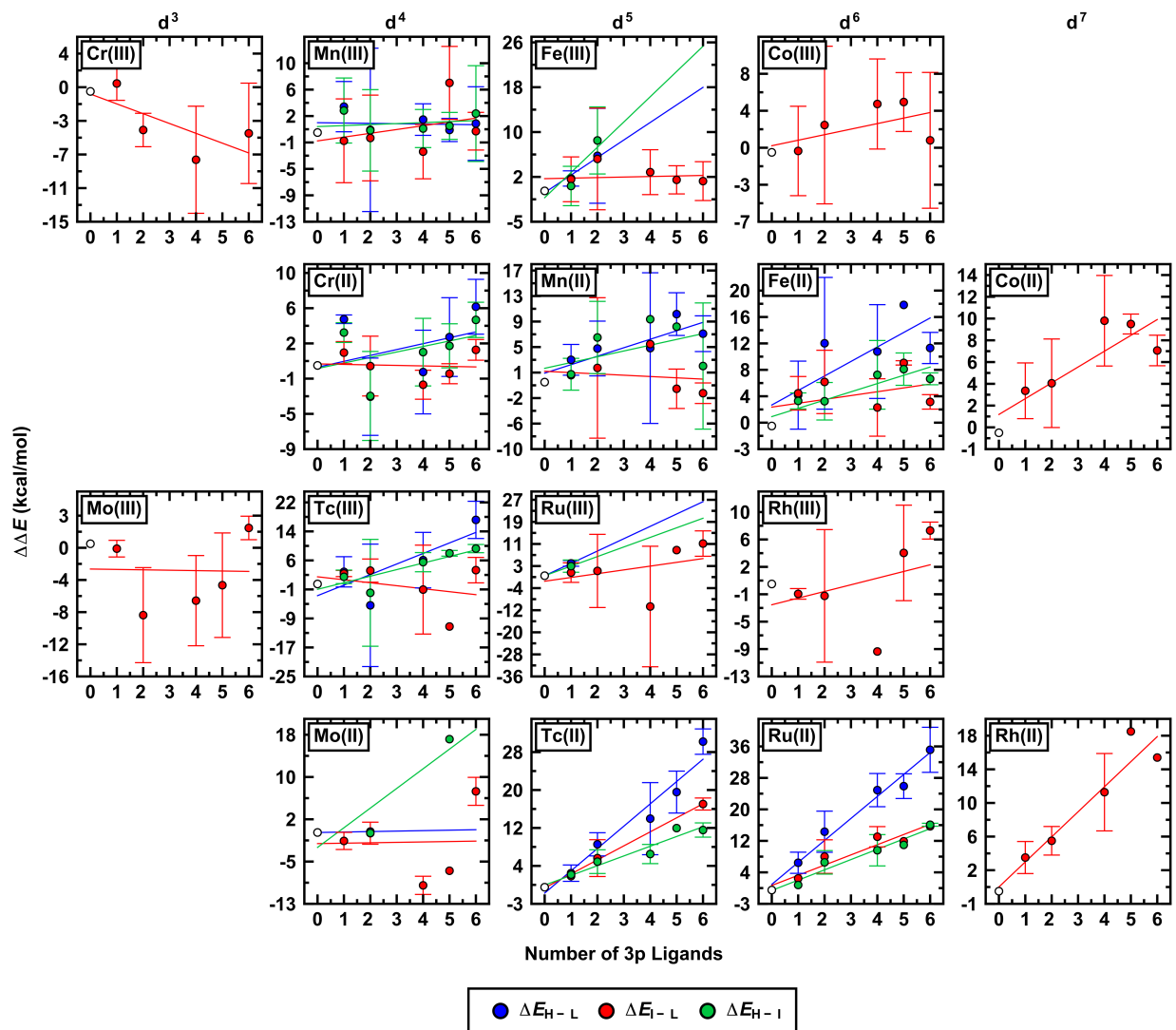


Figure S12. The change $\Delta\Delta E$ in spin-splitting energies, ΔE , in kcal/mol in the ILP data set for H-L (blue circles), I-L (red circles), and H-I (green circles) spin state comparisons. The data is subdivided by metal and oxidation state and reported as a function of the number of ligands undergoing $2p$ to $3p$ substitution (i.e., 1, 2, 4, 5, or 6 ligands). We include an additional point shown as a white circle at (0,0) when fitting trend lines with ordinary least squares through average values. The error bars shown are standard deviations evaluated over all available pairs. The range of the y-axis varies with metal type, and the clearest trends are apparent for later transition metals.

Table S15. Linear fits of the change in spin-splitting energies ($\Delta\Delta E$, y in kcal/mol) in the ILP data set as a function of the number of ligands undergoing $2p$ to $3p$ substitution (x). Best-fit lines are fit using ordinary least squares, and an R^2 is reported for each fit.

	Oxidation State II			Oxidation State III		
	ΔE_{H-L}	ΔE_{I-L}	ΔE_{H-I}	ΔE_{H-L}	ΔE_{I-L}	ΔE_{H-I}
Cr	$y = 0.669x - 0.204$ $R^2 = 0.165$	$y = -0.057x + 0.174$ $R^2 = 0.008$	$y = 0.624x - 0.345$ $R^2 = 0.238$		$y = -1.168x - 0.315$ $R^2 = 0.558$	
Mn	$y = 1.328x + 1.41$ $R^2 = 0.756$	$y = -0.205x + 1.698$ $R^2 = 0.03$	$y = 0.906x + 2.169$ $R^2 = 0.266$	$y = -0.051x + 1.494$ $R^2 = 0.007$	$y = 0.574x - 1.262$ $R^2 = 0.14$	$y = 0.151x + 0.906$ $R^2 = 0.065$
Fe	$y = 2.196x + 3.177$ $R^2 = 0.647$	$y = 0.582x + 2.858$ $R^2 = 0.175$	$y = 1.251x + 1.417$ $R^2 = 0.828$	$y = 3.13x - 0.304$ $R^2 = 0.972$	$y = 0.096x + 2.185$ $R^2 = 0.014$	$y = 4.503x - 1.21$ $R^2 = 0.822$
Co		$y = 1.454x + 1.682$ $R^2 = 0.744$			$y = 0.599x + 0.718$ $R^2 = 0.34$	
Mo	$y = 0.088x + 0.0$ $R^2 = 1.0$	$y = 0.078x - 2.101$ $R^2 = 0.001$	$y = 3.721x - 2.826$ $R^2 = 0.839$		$y = -0.049x - 3.141$ $R^2 = 0.001$	
Tc	$y = 4.704x - 1.239$ $R^2 = 0.952$	$y = 2.956x - 0.145$ $R^2 = 0.998$	$y = 2.051x + 0.446$ $R^2 = 0.942$	$y = 2.908x - 3.218$ $R^2 = 0.639$	$y = -0.822x + 1.986$ $R^2 = 0.108$	$y = 1.811x - 1.471$ $R^2 = 0.774$
Ru	$y = 5.587x + 1.44$ $R^2 = 0.979$	$y = 2.589x + 1.168$ $R^2 = 0.931$	$y = 2.616x - 0.095$ $R^2 = 0.957$	$y = 4.469x + 0.0$ $R^2 = 1.0$	$y = 1.369x - 2.002$ $R^2 = 0.162$	$y = 3.47x + 0.0$ $R^2 = 1.0$
Rh		$y = 2.981x + 0.504$ $R^2 = 0.925$			$y = 0.973x - 3.035$ $R^2 = 0.144$	

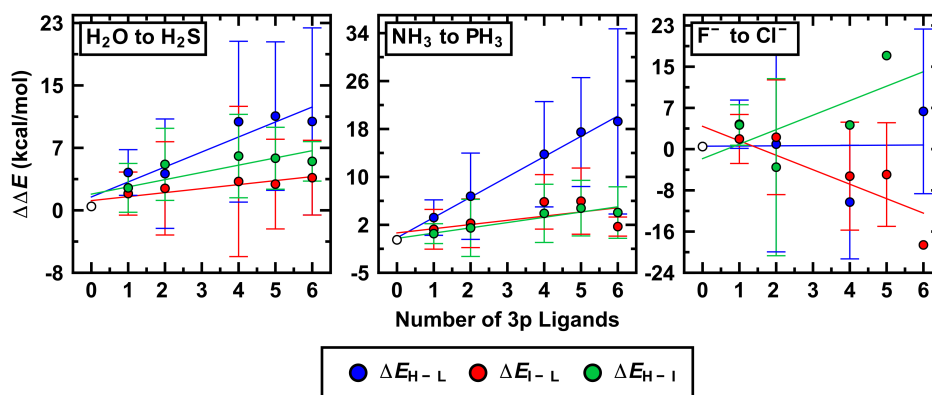


Figure S13. The change $\Delta\Delta E$ in spin-splitting energies, ΔE , in kcal/mol in the ILP data set as a function of the number of ligands undergoing $2p$ to $3p$ substitution (x , i.e., 1, 2, 4, 5, or 6 ligands), subdivided by the ligand undergoing substitution for H-L (blue circles), I-L (red circles), and H-I (green circles) spin state comparisons. The TMCs that include the simultaneous substitution of multiple ligand types are excluded. We include an additional point shown as a white circle at (0,0) when fitting trend lines with ordinary least squares through average values. The error bars shown are standard deviations evaluated over all available pairs.

Table S16. Linear fits of the change in spin-splitting energies ($\Delta\Delta E$, y in kcal/mol) in the ILP data set as a function of the number of ligands undergoing $2p$ to $3p$ substitution (x), subdivided by specific ligands undergoing substitution (indicated in left column). Best-fit lines are fit using ordinary least squares with a point at (0,0) included, and an R^2 is reported for each fit.

	ΔE_{H-L}	ΔE_{I-L}	ΔE_{H-I}
H ₂ O to H ₂ S	$y=1.92x+1.214$ $R^2=0.9$	$y=0.513x+0.744$ $R^2=0.842$	$y=0.927x+1.577$ $R^2=0.716$
NH ₃ to PH ₃	$y=3.388x+0.34$ $R^2=0.995$	$y=0.7x+1.155$ $R^2=0.404$	$y=0.878x+0.244$ $R^2=0.921$
F ⁻ to Cl ⁻	$y=0.039x+0.064$ $R^2=0.0$	$y=-2.809x+3.926$ $R^2=0.71$	$y=2.812x-2.344$ $R^2=0.511$

Table S17. The average difference in ΔE_{LD} in kcal/mol between TMCs with identical metals and axial ligands but with equatorial ligands that differ from $2p$ to $3p$ (i.e., H₂O/S₂O, NH₃/PH₃, or F⁻/Cl⁻). Positive values indicate that ΔE_{LD} is larger in TMCs with equatorial $3p$ ligands, and negative values indicate the opposite. Standard deviations for each subset are also shown.

Cr(III)	Cr(II)	Mn(III)	Mn(II)	Fe(III)	Fe(II)	Co(III)	Co(II)
4.82±7.88	6.67±9.31	-0.14±8.92	4.04±2.92	2.69±6.11	4.33±3.46	1.54±6.57	5.74±7.38
Mo(III)	Mo(II)	Tc(III)	Tc(II)	Ru(III)	Ru(II)	Rh(III)	Rh(II)
0.62±2.2	1.71±5.6	-2.4±8.79	-1.99±8.53	2.8±2.6	3.48±3.6	1.09±4.65	3.74±5.42

Table S18. The average difference in ΔE_{LD} in kcal/mol between TMCs with identical metals but either the two axial ligands (including the dissociated ligand) or the four equatorial ligands exchanged from $2p$ to the isovalent $3p$ (i.e., H₂O/S₂O, NH₃/PH₃, or F⁻/Cl⁻). Positive values indicate that ΔE_{LD} is larger in TMCs with $3p$ ligands, and negative values indicate the opposite. Standard deviations for each subset are also shown. No halides were computed because only neutral ligands were dissociated.

	Equatorial Substitution	Axial Substitution
H ₂ O to H ₂ S	0.64±6.53	-11.6±4.71
NH ₃ to PH ₃	2.78±7.43	-15.94±6.96
F ⁻ to Cl ⁻	4.58±6.15	no available data

Table S19. Average mean unsigned error (MUE, in kcal/mol) for ensembles of 25 models assigned to specific inter-row learning tasks (far left column) with particular model types (second column from left). The number of inter-row data points corresponds to the number of examples in the training set which come from the same row as the validation data.

		Inter-row Data Points					
		10	15	20	30	40	50
3d to 4d IMP ΔE_{H-L}	S-RACs	18.3	14.7	12.7	10.9	9.4	7.9
	S-eRACs	16.7	13.5	12.0	10.2	9.2	8.5
	T-RACs	13.7	12.4	10.8	9.9	8.8	8.3
	T-eRACs	11.0	10.0	9.1	8.4	7.8	7.4
2p to 3p ILP ΔE_{H-L}	S-RACs	16.9	12.6	11.3	9.8	8.8	7.1
	S-eRACs	15.8	14.6	13.0	11.1	10.1	9.4
	T-RACs	8.4	7.3	6.4	5.9	5.4	5.0
	T-eRACs	6.1	5.7	5.0	4.7	4.6	4.3
3d to 4d IMP ΔE_{LD}	S-RACs	15.6	14.7	13.3	11.6	10.4	9.6
	S-eRACs	15.8	14.6	13.0	11.1	10.1	9.4
	T-RACs	7.5	7.4	7.2	6.9	6.7	6.5
	T-eRACs	6.6	6.6	6.4	6.2	6.1	5.9
2p to 3p ILP ΔE_{LD}	S-RACs	13.1	12.3	11.3	10.0	9.0	8.1
	S-eRACs	13.4	12.4	11.2	9.8	8.6	7.9
	T-RACs	7.9	7.6	7.1	6.7	6.5	6.2
	T-eRACs	7.1	7.0	6.8	6.4	6.2	6.0

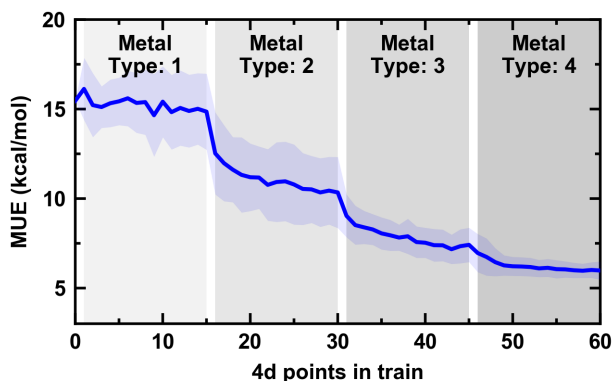


Figure S14. Mean unsigned error (MUE, in kcal/mol) results for the $3d$ to $4d$ learning task in the IMP data set on the ΔE_{I-L} property when the $4d$ metals are grouped by type with a T-eRAC KRR model. The blue translucent shaded region represents the standard deviation of an ensemble of 25 models. For each model, the $4d$ metal types (Mo, Tc, Ru, Rh) are arranged in a random order, and 15 data points corresponding to each metal are added before adding the next metal, as indicated by the gray shaded regions and white separators.

Table S20. Average mean unsigned errors (MUE, in kcal/mol) from an ensemble of 25 models for the typed inter-row learning task with a T-eRAC KRR model. Values are obtained for predicting the ΔE_{I-L} property in the IMP data set for the $3d$ to $4d$ learning task. In typed inter-row learning, the $4d$ metals (Mo, Tc, Ru, Rh) are arranged in a random order, and 15 data points corresponding to each metal are added before moving to the next metal. We report the average MUE across the first 5 examples of each metal, the middle 5 examples, and the last 5 examples. We also report the average of all 15 MUEs for each metal added.

	First 5	Middle 5	Last 5	Average of all 15 MUEs
Metal 1	15.4	15.3	14.9	15.2
Metal 2	11.7	10.9	10.4	11.0
Metal 3	8.5	7.8	7.3	7.8
Metal 4	6.5	6.1	6.0	6.2

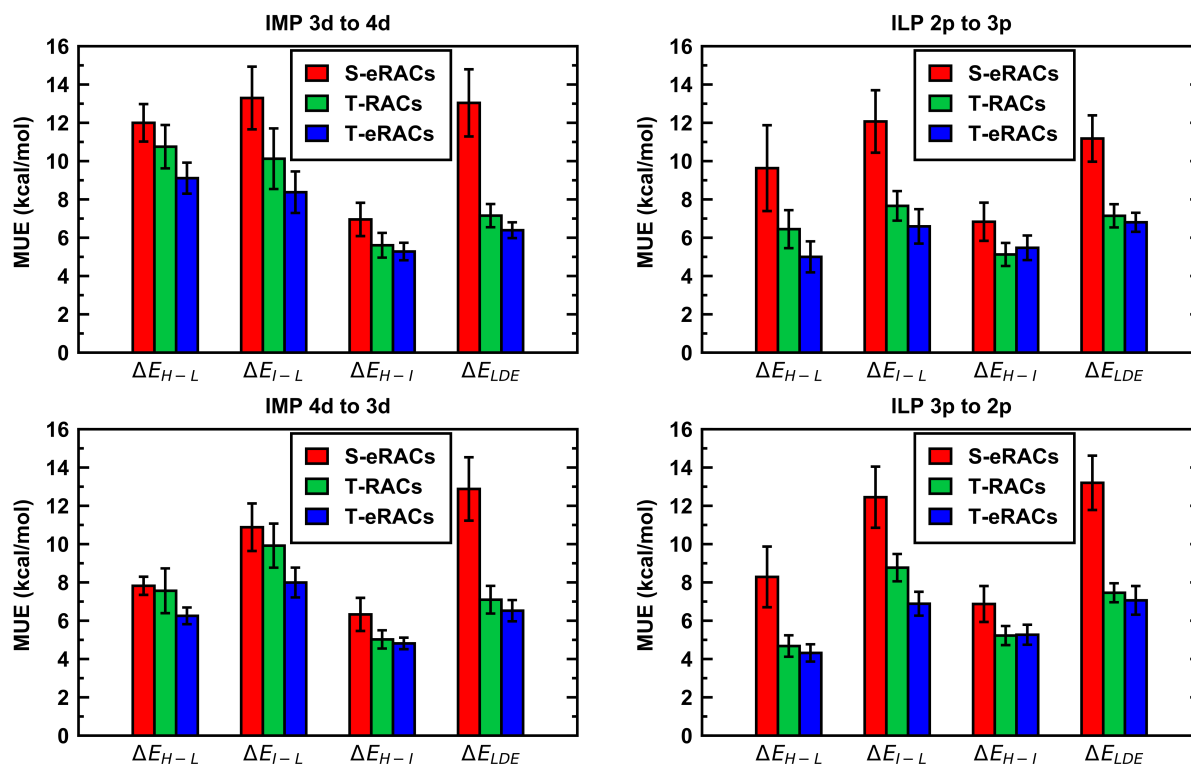


Figure S15. Mean unsigned error (MUE, in kcal/mol) results in a grouped bar graph by property (i.e., ΔE_{H-L} , ΔE_{I-L} , ΔE_{H-I} , or ΔE_{LDE}) for each of the four learning tasks: learning $4d$ properties based on $3d$ data in the IMP data set (top left), learning $3p$ properties based on $2p$ data in the ILP data set (top right), learning $3d$ properties based on $4d$ data in the IMP data set (bottom left), and learning $2p$ properties based on $3p$ data in ILP data set (bottom right). The average of model performance is shown as the bar, the standard deviation over the ensemble is shown as an error bar, and the nature of the model (i.e., S-eRACs, T-RACs, or T-eRACs) is colored according to inset legend. In each case, the training set includes all available data from the alternate row of the periodic table, and the T models are also trained on 20 examples from the same row as the validation data.

Table S21. Mean unsigned error (MUE, in kcal/mol) for KRR model predictions with the average MUE of a 25-model ensemble shown along with its standard deviation. Results are reported for each of the four learning tasks, with four properties and three model types in each case. In each case, the training set includes all available data from the alternate row of the periodic table, and the T models are also trained on 20 examples from the same row as the validation data.

	ΔE_{H-L}	ΔE_{I-L}	ΔE_{H-I}	ΔE_{LD}
IMP 3d to 4d				
S-eRACs	12.0±0.98	13.3±1.64	6.95±0.87	13.04±1.75
T-RACs	10.75±1.13	10.12±1.58	5.61±0.65	7.15±0.61
T-eRACs	9.11±0.81	8.38±1.08	5.28±0.46	6.39±0.41
ILP 2p to 3p				
S-eRACs	9.63±2.24	12.07±1.63	6.83±1.0	11.18±1.21
T-RACs	6.45±0.99	7.66±0.77	5.13±0.6	7.14±0.61
T-eRACs	5.0±0.81	6.59±0.9	5.47±0.64	6.81±0.5
IMP 4d to 3d				
S-eRACs	7.82±0.47	10.88±1.24	6.33±0.86	12.88±1.65
T-RACs	7.56±1.17	9.92±1.15	5.02±0.48	7.1±0.72
T-eRACs	6.25±0.44	7.99±0.78	4.81±0.3	6.52±0.55
ILP 3p to 2p				
S-eRACs	8.29±1.58	12.45±1.6	6.87±0.94	13.2±1.42
T-RACs	4.68±0.56	8.77±0.71	5.23±0.5	7.46±0.5
T-eRACs	4.32±0.45	6.89±0.62	5.27±0.52	7.06±0.75

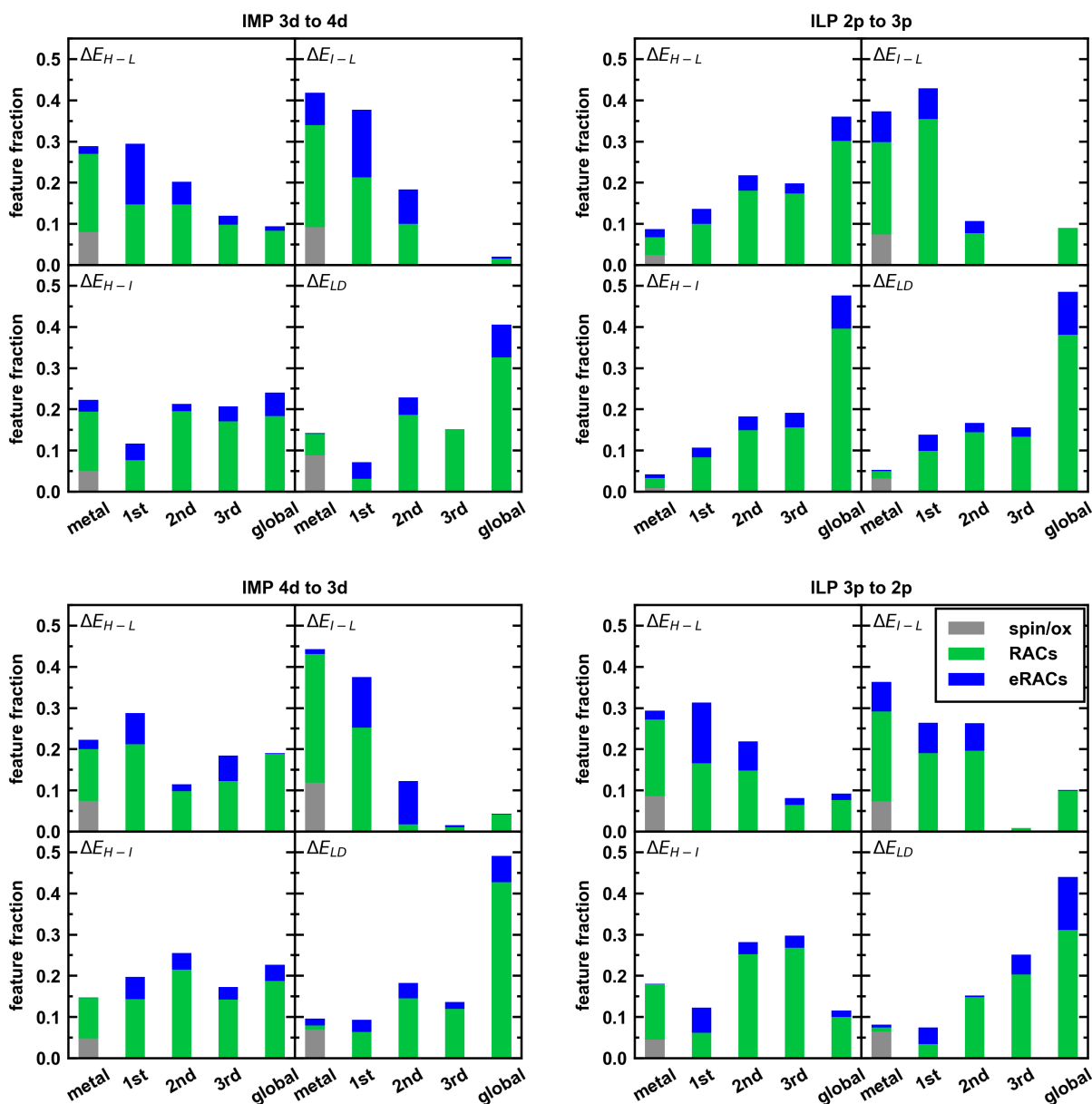


Figure S16. Fraction of features selected as a stacked bar chart in both the IMP (top) and ILP (bottom) data set when training models for all properties considered in this work (i.e., ΔE_{H-L} , ΔE_{I-L} , ΔE_{H-I} , ΔE_{LD}). In each case, 25 models are trained using 20 training points from the same row as the validation data and all data from the opposite row (i.e., T-eRAC models). Features are grouped by the atom that is most distant from the metal (0, 1, 2, 3, or > 3 bonds away) in the feature. Features are colored based on whether they are not based on autocorrelations (gray, spin/ox), are standard autocorrelation features in RAC-155 (green, RACs), or are derived from the Z_{eff} atomic property (blue, eRACs).

Table S22. Average fraction of features by heuristic property type in the feature-selected eRAC-185 subspace of the 25 KRR models used to build the ensemble for each property and data set indicated in the left two columns of the table below. Feature fractions are normalized prior to averaging across the 25 models, and any models that used the full representation (i.e., in lieu of LASSO or 1% RF cutoff) are excluded.

		ox/spin	Z _{eff}	chi	Z	T	I	S
IMP <i>3d to 4d</i>	ΔE_{H-L}	0.08	0.25	0.26	0.32	0.02	0.01	0.07
	ΔE_{I-L}	0.09	0.33	0.20	0.27	0.00	0.00	0.10
	ΔE_{H-I}	0.05	0.18	0.21	0.33	0.02	0.05	0.16
	ΔE_{LD}	0.09	0.17	0.27	0.16	0.04	0.05	0.24
ILP <i>2p to 3p</i>	ΔE_{H-L}	0.02	0.18	0.22	0.22	0.12	0.07	0.17
	ΔE_{I-L}	0.07	0.18	0.21	0.34	0.00	0.00	0.20
	ΔE_{H-I}	0.01	0.18	0.18	0.19	0.15	0.11	0.18
	ΔE_{LD}	0.03	0.19	0.19	0.17	0.12	0.10	0.19
IMP <i>4d to 3d</i>	ΔE_{H-L}	0.08	0.18	0.26	0.36	0.01	0.02	0.11
	ΔE_{I-L}	0.12	0.25	0.21	0.24	0.00	0.00	0.18
	ΔE_{H-I}	0.05	0.16	0.26	0.35	0.04	0.05	0.10
	ΔE_{LD}	0.07	0.16	0.32	0.13	0.09	0.07	0.15
ILP <i>3p to 2p</i>	ΔE_{H-L}	0.09	0.27	0.26	0.3	0.03	0.01	0.04
	ΔE_{I-L}	0.07	0.21	0.26	0.31	0.00	0.00	0.14
	ΔE_{H-I}	0.05	0.14	0.28	0.27	0.04	0.02	0.21
	ΔE_{LD}	0.06	0.23	0.18	0.22	0.06	0.07	0.18

Table S23. Average fraction of features categorized by the shortest bond path between the metal center and the most distant atom in the feature (i.e., 0, 1, 2, 3, or more and labeled as metal, 1st, 2nd, 3rd, or global) in the feature-selected eRAC-185 subspace of the 25 KRR models used to build the ensemble for each property and data set indicated in the left two columns of the table below. Feature fractions are normalized prior to averaging across the 25 models, and any models that used the full representation (i.e., in lieu of LASSO or 1% RF cutoff) are excluded.

		metal	1st	2nd	3rd	global
IMP 3d to 4d	ΔE_{H-L}	0.29	0.29	0.20	0.12	0.09
	ΔE_{I-L}	0.42	0.38	0.18	0.00	0.02
	ΔE_{H-I}	0.22	0.12	0.21	0.21	0.24
	ΔE_{LD}	0.14	0.07	0.23	0.15	0.41
ILP 2p to 3p	ΔE_{H-L}	0.09	0.14	0.22	0.20	0.36
	ΔE_{I-L}	0.37	0.43	0.11	0.00	0.09
	ΔE_{H-I}	0.04	0.11	0.18	0.19	0.48
	ΔE_{LD}	0.05	0.14	0.17	0.16	0.49
IMP 4d to 3d	ΔE_{H-L}	0.22	0.29	0.12	0.18	0.19
	ΔE_{I-L}	0.44	0.38	0.12	0.02	0.04
	ΔE_{H-I}	0.15	0.20	0.26	0.17	0.23
	ΔE_{LD}	0.10	0.09	0.18	0.14	0.49
ILP 3p to 2p	ΔE_{H-L}	0.29	0.31	0.22	0.08	0.09
	ΔE_{I-L}	0.36	0.26	0.26	0.01	0.10
	ΔE_{H-I}	0.18	0.12	0.28	0.30	0.12
	ΔE_{LD}	0.08	0.07	0.15	0.25	0.44

Table S24. Average distance between TMCs in the eRAC-185 and RAC-155 feature-selected subspaces of trained models for $3d$ to $4d$ in the IMP data set. TMCs are subdivided by the metal identity. The averages are weighted such that each of the 25 KRR models contributes equally, and distances are normalized such that the average distance between any two TMCs is 1.

	RAC-155									eRAC-185							
	Cr	Mn	Fe	Co	Mo	Tc	Ru	Rh		Cr	Mn	Fe	Co	Mo	Tc	Ru	Rh
ΔE_{H-L}	Cr	0.86	0.93	0.90		1.05	1.12	1.08		0.60	0.82	1.01		1.05	1.16	1.32	
	Mn	0.93	0.89	0.92		1.1	1.08	1.1		0.82	0.74	0.89		1.18	1.13	1.26	
	Fe	0.90	0.92	0.87		1.02	1.06	1.01		1.01	0.89	0.74		1.22	1.12	1.07	
	Co																
	Mo	1.05	1.10	1.02		0.89	0.98	0.94		1.05	1.18	1.22		0.65	0.87	1.05	
	Tc	1.12	1.08	1.06		0.98	0.93	1.00		1.16	1.13	1.12		0.87	0.79	0.94	
	Ru	1.08	1.10	1.01		0.94	1.00	0.91		1.32	1.26	1.07		1.05	0.94	0.79	
	Rh																
ΔE_{L-L}	Cr	0.58	0.71	0.64	0.67	1.22	1.41	1.30	1.39	0.52	0.70	0.85	1.09	1.03	1.24	1.26	1.48
	Mn	0.71	0.61	0.78	0.81	1.26	1.31	1.39	1.49	0.70	0.57	0.79	0.97	1.11	1.12	1.24	1.42
	Fe	0.64	0.78	0.56	0.58	1.09	1.31	1.12	1.21	0.85	0.79	0.58	0.68	1.10	1.18	0.99	1.10
	Co	0.67	0.81	0.58	0.57	1.03	1.26	1.07	1.16	1.09	0.97	0.68	0.59	1.27	1.27	1.01	1.03
	Mo	1.22	1.26	1.09	1.03	0.67	0.87	0.78	0.81	1.03	1.11	1.10	1.27	0.57	0.81	0.91	1.15
	Tc	1.41	1.31	1.31	1.26	0.87	0.68	1.09	1.12	1.24	1.12	1.18	1.27	0.81	0.62	1.00	1.16
	Ru	1.30	1.39	1.12	1.07	0.78	1.09	0.67	0.70	1.26	1.24	0.99	1.01	0.91	1.00	0.63	0.73
	Rh	1.39	1.49	1.21	1.16	0.81	1.12	0.70	0.69	1.48	1.42	1.10	1.03	1.15	1.16	0.73	0.65
ΔE_{H-I}	Cr	0.81	0.92	0.89		1.03	1.12	1.09		0.75	0.90	0.98		1.01	1.13	1.18	
	Mn	0.92	0.87	0.92		1.1	1.08	1.11		0.90	0.83	0.93		1.11	1.07	1.15	
	Fe	0.89	0.92	0.86		1.03	1.07	1.02		0.98	0.93	0.83		1.12	1.1	1.02	
	Co																
	Mo	1.03	1.1	1.03		0.84	0.96	0.93		1.01	1.11	1.12		0.78	0.95	1.02	
	Tc	1.12	1.08	1.07		0.96	0.91	0.99		1.13	1.07	1.10		0.95	0.86	1.01	
	Ru	1.09	1.11	1.02		0.93	0.99	0.90		1.18	1.15	1.02		1.02	1.01	0.87	
	Rh																
ΔE_{D}	Cr	0.95	0.96	0.95	0.95	1.03	1.05	1.04	1.05	0.93	0.96	0.97	1.01	1.00	1.05	1.04	1.10
	Mn	0.96	0.95	0.97	0.97	1.04	1.04	1.05	1.07	0.96	0.93	0.97	1.00	1.03	1.03	1.05	1.10
	Fe	0.95	0.97	0.94	0.94	1.01	1.03	1.00	1.02	0.97	0.97	0.92	0.94	1.01	1.03	0.97	1.00
	Co	0.95	0.97	0.94	0.93	1.00	1.02	1.00	1.00	1.01	1.00	0.94	0.92	1.04	1.05	0.97	0.97
	Mo	1.03	1.04	1.01	1.00	0.97	0.99	0.98	0.98	1.00	1.03	1.01	1.04	0.93	0.98	0.98	1.02
	Tc	1.05	1.04	1.03	1.02	0.99	0.97	1.01	1.01	1.05	1.03	1.03	1.05	0.98	0.94	1.01	1.05
	Ru	1.04	1.05	1.00	1.00	0.98	1.01	0.96	0.96	1.04	1.05	0.97	0.97	0.98	1.01	0.93	0.94
	Rh	1.05	1.07	1.02	1.00	0.98	1.01	0.96	0.96	1.10	1.10	1.00	0.97	1.02	1.05	0.94	0.93